Investigations in the food-energy-water nexus: The effects of mixed wettability on soil evaporation and the feasibility of using nuclear microreactor process heat for concurrent bioconversion and agricultural practices

by

Jack Pakkebier

B.S., Fort Hays State University, 2022

A THESIS

submitted in partial fulfillment of the requirements for the degree

MASTER OF SCIENCE

Alan Levin Department of Mechanical and Nuclear Engineering
Carl R. Ice College of Engineering

KANSAS STATE UNIVERSITY
Manhattan, Kansas

2024

Approved by:

Major Professor
Dr. Melanie M. Derby

Copyright

Abstract

Food, energy, and water are inherently connected. The Ogallala Aquifer, a primary irrigation water source in the High Plains region of the U.S., is declining, thereby necessitating new water conservation strategies[1]. Meanwhile, there is also a global goal to achieve a 43% reduction in global greenhouse gas emissions by 2030, relative to the levels recorded in 2019[2]. These problems are separate yet still interconnected. The work of this thesis poses solutions in which these problems may be alleviated.

First, this thesis investigates the impacts of mixed wettability on the evaporation dynamics of a 10-μL sessile water droplet placed within simulated soil pores comprised of hydrophobic Teflon beads (CA ~ 108°) and hydrophilic glass (CA ~ 41°) beads with 2.38-mm diameters, where homogeneous and heterogeneous (i.e., mixed hydrophobicity and hydrophilicity) wettability configurations were investigated. Mixed wettability was of particular interest due to the possibility of reaping the lengthened evaporation times of hydrophobic materials[3] while also having the advantages of decreased runoff and enhanced infiltration attributed to hydrophilic materials[4,5]. Experiments were performed in an environmental chamber where the relative humidity and temperature were $60\% \pm 0.1\%$ RH and $20°\text{C} \pm 0.4°\text{C}$, respectively. Wettability influenced evaporation times, with homogeneous hydrophobic pores (i.e., three Teflon beads) and heterogeneous one glass, two Teflon pores having the longest average evaporation times of 40 and 39 minutes, respectively. Homogeneous hydrophilic pores (i.e., three glass beads) and heterogeneous two glass, one Teflon pores exhibited evaporation times of 34 minutes. Evaporation times for heterogeneous combinations trended based on the predominant wettability. Contact angles and the projected length of contact were analyzed from videos to capture pinning and

depinning during evaporation. For many measurements on hydrophobic beads, contact angles were less than 90°, and in some configurations, water would be pinned on a Teflon bead while depinning (i.e., moving) on a glass bead. Stick-slip evaporation was observed, where the evaporating droplet switched between constant contact radius (CCR) and constant contact area (CCA) evaporative modes to minimize droplet surface energy. The results suggest wettability alterations in agricultural settings may reduce evaporation.

For the next portion of the thesis, the feasibility of using nuclear microreactor process heat for bioconversion and agricultural processes is investigated. Nuclear microreactors, a subset of small modular reactors, offer promise in addressing climate challenges due to their compact size, ease of deployment, and potential for carbon-neutral power generation. Operational conditions and requirements of bioconversion and agricultural methods (e.g., gasification, pyrolysis, hydrothermal carbonization, hydrothermal liquefaction, hydrothermal gasification, ethanol production, anaerobic digestion, and pasteurization) are obtained from a brief literature review. Next, a Brayton cycle model with a regenerator and air as the working fluid, based on the eVinci microreactor design[6], was developed to assess the feasibility of powering these processes using nuclear microreactor heat. Exergetic efficiency values were calculated to match process heat values with operational temperatures, where high-temperature processes such as gasification and pyrolysis demonstrated efficiencies of 72-100% and lower-temperature processes such as pasteurization and anaerobic digestion ranged from 2-53%, depending on the microreactor design. There were tradeoffs between producing net power and utilizing process heat, particularly for high-temperature processes; three different heat exchanger locations were considered. Results show that high-temperature processes [e.g., gasification (600℃ at minimum)] require too high of temperatures to be feasible based on the model. Some processes (e.g., ethanol production, hydrothermal carbonization, and hydrothermal liquefaction) are more suited to a heat exchanger located between the turbine and regenerator, but can also be run before the turbine. Lower temperature processes, like pasteurization and anaerobic digestion, can utilize waste heat after the regenerator and, therefore, do not impact power production.

Table of Contents

List of Figures

List of Tables

Acknowledgments

I gratefully acknowledge Dr. Derby for her role as a supportive and steadfast advisor, the Institute for Environmental Research at Kansas State University for the use of their environmental chambers, and my lab mates who motivated me to stay the path. I would also like to thank Partha Chakraborty for his invaluable assistance in the conceptualization and reviewing of the work on mixed wettability, and Christopher Skangos for his support in the development and refinement of the work over microreactor feasibility.

This work was supported by the National Science Foundation grant numbers 1828571 and 165141, and by the Department of Energy Nuclear Energy University Programs under grant no. DE-NE0009152.

Dedication

For my family, always.

Preface

The abstract, chapter 1, and chapter 2 contain work reproduced from

> Jack Pakkebier, Partha P. Chakraborty, Melanie M. Derby; Effects of heterogenous wettability on evaporation from a simulated soil pore: Stick-slip evaporative mode and contact line motion. *AIP Advances* 1 March 2024; 14 (3): 035127. https://doi.org/10.1063/5.0193326,

with the permission of AIP Publishing.

Chapter 1 - Introduction

Food, energy, and water (FEW) constitute three fundamental resources crucial for humans, but they confront increasing demand and finite availability, posing significant global challenges[7]. Simultaneously, there exists an intrinsic linkage among food, energy, and water. This concept is symbolically known as the FEW nexus, suggesting that restrictions or bottlenecks affecting one resource could restrict the accessibility of others[8]. The FEW nexus is heavily impacted by the proliferation of climate change[9]. Without specific policies to mitigate greenhouse emissions, by the end of the 21st century, global mean temperatures are projected to rise between 1.6℃ and 6.9℃ compared to the 1980-1999 average[10]. Preserving and protecting the natural resources, health, and beauty of the Earth as populations increase and cultures modernize is a problem facing modern society. Due to this, legislation such as the Paris Agreement is being developed to limit the increase of global average temperature to 1.5℃[11]. To recognize this, there is a target to achieve a 43% reduction in global greenhouse gas emissions by 2030, compared to that of 2019 levels[2]. So far, only 4.5% of countries have achieved carbon neutrality, and most plan to do so by 2050-2070[12,13].

If global temperatures continue to increase, this will only proliferate other existing problems such as agricultural water management. The Ogallala Aquifer spans a major portion of the High Plains Aquifer, which underlies 45 million ha (111 million acres) of land in Wyoming, South Dakota, Nebraska, Kansas, Colorado, Oklahoma, Texas, and New Mexico[14]. The Ogallala Aquifer accounts for approximately 30% of all irrigation in the US[15], and with the Ogallala Aquifer currently declining, it is projected that 40% and 54% of currently irrigated land in the central and southern High Plains, respectively, will no longer be viable for irrigation by the end of the 21st century[16]. The depletion of the Ogallala Aquifer thereby requires alternative water conservation strategies, and in this thesis, the impacts of wettability to alter evaporation mechanisms are explored as a potential solution. This is due to wettability's ability to impact sessile and mobile droplet evaporation. In particular, this work considers mixed (i.e., heterogeneous) wettability which is the case where hydrophobic (contact angle > 90°) and hydrophilic (contact angle < 90°) substances interact with each other. Purely hydrophobic soil structures are attributed with increased water runoff but higher water retention while hydrophilic soil structures exhibit the reverse[4,5]. Due to this contrast, mixed wettability is of particular interest for leveraging the best attributes of each wettability. Currently, research exploring the effects of implementing mixed wettability[17–19] on evaporation mechanics is less prevalent compared to that of homogeneous wettability[20–24]. Experiments were conducted to determine the impact of mixed wettability on evaporation times, contact angles, the projected length of contact, and evaporative modes.

Another opportunity to address these concerns is to incorporate carbon-neutral power sources in industrial processes to reduce carbon dioxide emissions[25,26]. An emerging carbon-neutral technology is that of nuclear microreactors, which can produce both heat and electricity on a smaller scale compared to a typical nuclear power plant[27]. Along with electrical production, the excess heat from nuclear microreactor designs can be utilized to power a large variety of bioconversion and agricultural processes, further promoting environmental sustainability. These processes include but are not limited to gasification, hydrothermal gasification (HTG), pyrolysis, hydrothermal liquefaction (HTL), hydrothermal carbonization (HTC), ethanol production, pasteurization, and anaerobic digestion (AD).

Chapter 2 - The Impacts of Mixed Wettability[1]

2.1 Literature Review

Philip and De Vries[28] developed a pioneering model to explain evaporation via water vapor diffusion in porous media under temperature gradients, in which the observed apparent vapor transfer was higher than predictions of Fick's law. The enhanced vapor diffusion was explained by the presence of liquid islands (i.e., water formed between two particles) that facilitate the movement of moisture through porous media. Subsequent work on the liquid island theory explained the contributions of latent heat transfer to the temperature-dependent behavior of thermal conductivity by Cass et al.[29] and Sakaguchi et al.[30] Also, liquid islands have been studied intensively by researchers such as Pepin et al.[31] and Darabi et al.[32] where they sought to estimate the time of liquid island rupture, which is part of the evaporation process.

Sessile droplet evaporation plays a role in a wide range of applications, including DNA/RNA micro-arrays deposition[33,34], dropwise evaporative cooling[35,36], ink-jet printing[37,38], pesticide spraying[39,40], micro/nanomaterial fabrication[41,42], and thin film coatings[42,43]. Wettability can impact sessile droplet evaporation. Research over the effects of implementing mixed (i.e., heterogeneous) wettability[17–19] on evaporation mechanics is less prevalent compared to that of homogeneous wettability[20–24]. The contact angle, CA, that forms between the solid and the liquid interface is a thermodynamic feature indicative of solid surface wettability, holding significant relevance in evaluating surfaces[44]. Despite its seemingly straightforward concept and extensive research history, the measurement and understanding of contact angles still face challenges due to

[1] Figures and parts of section originally published in Jack Pakkebier, Partha P. Chakraborty, Melanie M. Derby; Effects of heterogenous wettability on evaporation from a simulated soil pore: Stick-slip evaporative mode and contact line motion. *AIP Advances* 1 March 2024; 14 (3): 035127. https://doi.org/10.1063/5.0193326

inadequate experimental and theoretical methodologies[45–47]. Mixed or heterogeneous wettability is the case where hydrophobic (CA > 90°) and hydrophilic (CA < 90°) substances interact with each other. Continued development into the study of mixed wettability may lead to the ability to be able to reap the benefits of both hydrophobic and hydrophilic substrates concurrently[48]. Therefore, a hypothetical heterogeneous surface may be able to have self-cleaning properties indicative of hydrophobic media[49], while also being able to form a liquid puddle, allowing solutes to be evenly deposited on the surface after evaporation[50]. Betz et al.[51] conducted research on mixed wettability where their development of superbiphilic surfaces displayed exceptional performance in pool boiling, indicated by biphilic surfaces demonstrating higher heat transfer coefficients compared to homogeneous wettability surfaces. Similarly, while investigating flow condensation heat transfer, Derby et al.[52] observed heat transfer coefficients on hydrophobic and mixed wettability patterned surfaces significantly that were greater than that of hydrophilic surfaces. Additionally, previous research has shown that hydrophilic surfaces and porous media exhibit shorter evaporation times compared to that of hydrophobic ones [3,17,53], as hydrophobicity alters exposed droplet-air surface areas. For a single simulated soil pore, Chakraborty et al.[53] determined that a hydrophobic Teflon pore exhibited a 23.5% longer evaporation time on average compared to that of a hydrophilic glass pore. In an experimental analysis regarding the dynamic effects of mixed wettability, Aboubakri et al.[18] concluded that the evaporation rate of a droplet on surfaces of mixed wettability is a function of the shape and the size of the evaporative medium. Similarly, Ustohal et al.[54] observed that surfaces of differing wettability dominate the water retention behavior in mixed packings. This further motivates the need to explore the impacts of mixed wettability and its effects on evaporation and water retention.

In addition to differing evaporation rates, evaporation modes in hydrophobic media differ compared to hydrophilic media. Picknett and Bexon[55] identified two distinct evaporative modes: constant contact angle evaporative mode (CCA) and constant contact radius evaporative mode (CCR). The CCA mode is often characterized by the droplet being depinned (i.e., a moving contact line), whereas the CCR mode is characterized as being pinned (i.e., a fixed contact line). The triple contact line refers to the line where the liquid droplet, the vapor phase, and the solid substrate meet, i.e. the interface formed at the periphery of the droplet on a solid surface. Later, a third evaporative mode was observed, referred to as the "stick-slip" evaporative mode[56]. In this evaporative mode, mixed evaporation behavior is seen where the liquid droplet exhibits both CCA and CCR modes intermittently. During the stick-slip evaporative mode, the triple contact line may remain pinned until the contact angle is reduced to a critical value. Once this critical value is achieved, the triple contact line resumes motion or rapidly retracts to the next equilibrium state, with corresponding changes in droplet apex height and contact angle[57]. Each one of these events is associated with an intrinsic energy barrier being surmounted. On smooth, flat hydrophobic surfaces, evaporation is generally characterized by the CCA mode[58], and for smooth, flat hydrophilic surfaces, the CCR mode is common[59].

Orejon et al.[60] studied contact line motion for evaporating water and ethanol droplets on a range of surfaces where they derived an equation using Young's equation and a force balance approach to predict the threshold of depinning,

$$\frac{\partial U}{\partial r} = \delta \vec{F} = \gamma sin(\theta_o)\delta\theta \qquad (2.1)$$

where θ_o is the equilibrium contact angle, $\delta\theta$ is a small change in the contact angle due to evaporation, γ is the liquid-vapor interfacial energy, and U is the intrinsic energy barrier preventing contact line motion. In other work, Picknett and Bexon[55] calculated the rate of evaporation for sessile droplets in the CCA model, and later Schönfeld[61] produced two approximations for the rate of evaporation in the CCR mode. These results were found by applying a liquid droplet onto a flat substrate and observing the contact angles throughout the evaporation process.

2.2 Research Objectives

In pursuit of a better understanding of how wettability affects evaporation mechanics, we applied a 10-μL liquid droplet of water onto a three-dimensional simulated soil pore comprised of three separate 2.38-mm diameter beads. The research objectives of this chapter are to investigate and compare the evaporation dynamics of sessile water droplets within simulated soil pores with varying wettability, including both homogeneous and heterogeneous configurations. This work aims to determine the impacts of mixed wettability on evaporation times, evolving contact angles and lines, and evaporative modes, with a focus on understanding the potential implications for agricultural water management.

2.3 Methods and Experimental Approach

The evaporation of a sessile water droplet was observed over the entire course of its evaporation. A 10-μL droplet of water was dispensed from a pipette (Fisherbrand Elite 00010, ± 1-2.5% accuracy). For clearer imaging and analysis, the water was dyed using red food coloring (i.e., < 2% of droplet volume). The droplet was placed in the middle of a simulated soil pore composed of three beads of varying wettability (Figure 2.1): 2.38-mm diameter hydrophobic polytetrafluoroethylene (PTFE) Teflon (CA ~ 108°) and hydrophilic glass (CA ~ 41°). The beads were held at an equilateral spacing of approximately 3.15 mm center-to-center by a 3D-printed fixture that suspends the beads via a removable adhesive, and new beads were used for each trial. All trials were conducted in a closed, environmental chamber where the relative humidity and temperature were set to be constant at $60\% \pm 0.1\%$ RH and $20°C \pm 0.4°C$, respectively.

Evaporation was observed by two high-speed cameras recording at 24 frames per second with a magnification of 5x (Fastec IL3 and Fastec IL5). The footage was simultaneously recorded from the top and side of the pore and was subsequently processed with ImageJ, SolidWorks, and Active Presenter (Atomi Systems). Four different wettability arrangements were tested: homogenous hydrophilic (i.e., 0 glass beads), heterogeneous wettability (i.e., 1 glass bead and 2 Teflon beads, and 2 glass beads and 1 Teflon bead), and homogenous hydrophobic (i.e., 3 Teflon beads). Five evaporation trials for each arrangement were conducted where the evaporation time, liquid island formation time, average evaporation time, and average liquid island formation time were reported.

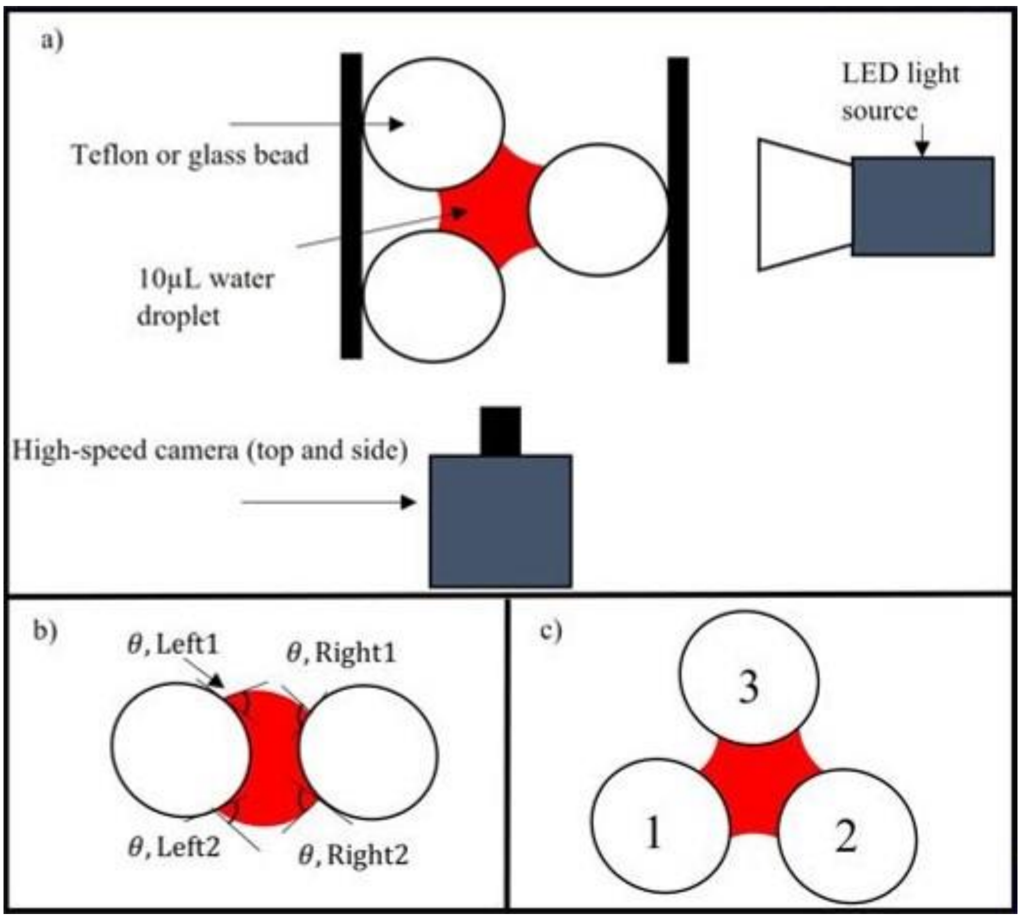

Figure 2.1: Schematic of experimental apparatus in the environmental chamber. (a) Top view of simulated pore with lighting and cameras. (b) Side view of simulated pore with contact angle description and notation. (c) Top view notation for beads.[62]

2.4 Results and Discussion

Representative images from the experimental videos are reported in Figure 2.2 at three different times during the experimental process: initial drop placement, immediately before liquid island formation, and immediately after liquid island formation. Images and videos from all trials are in Appendix A.

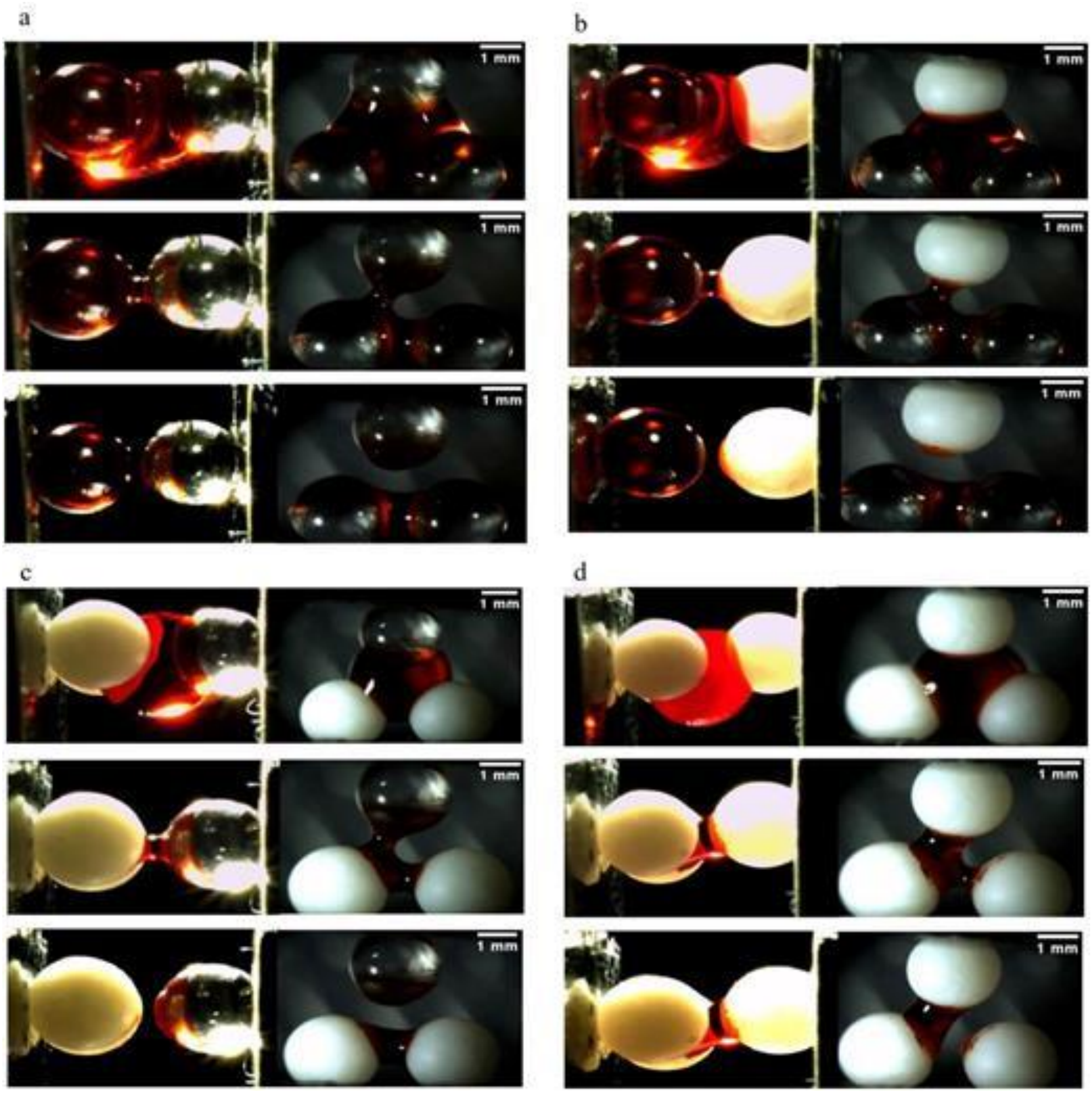

Figure 2.2: Evaporation in a simulated soil pore for the different wettability configurations for initial droplet placement, immediately before liquid island formation, and immediately after liquid island formation, where (a): homogenous hydrophilic, 3 glass 0 Teflon; (b):

heterogeneous wettability, 2 glass 1 Teflon; (c): heterogeneous wettability, 1 glass 2 Teflon, and (d): homogenous hydrophobic, 0 glass 3 Teflon.[62]

In each arrangement, the topmost image is the initial droplet placement. Then, the middle picture is immediately before liquid island formation and the bottom picture is the formed liquid island, where evaporation will continue until the water is completely evaporated. The data in Table 1 indicate that the homogeneous hydrophilic (3 glass) and heterogeneous wettability (2 glass 1 Teflon) arrangements had the shortest average evaporation times of 34 ± 4.5 minutes and 34 ± 4.2 minutes, respectively. These values represent the average evaporation time ± standard deviation. In contrast, the homogenous hydrophobic (3 Teflon) arrangement had the longest average evaporation time of 40 ± 4.8 minutes, and the second longest average evaporation time was that of the heterogeneous wettability (1 glass 2 Teflon) arrangement at 39 ± 4.2 minutes. The noticeable standard deviation between experimental trials may be a result of slight droplet placement variabilities and the pipette's accuracy of ± 1-2.5%.

Table 2.1: Evaporation times for all wettability combinations.[62]

Homogenous hydrophilic (3 glass 0 Teflon)			Heterogeneous wettability (2 glass 1 Teflon)		
Trial	Liquid Island Formation (minutes)	Evaporation (minutes)	Trial	Liquid Island Formation (minutes)	Evaporation (minutes)
1	22	26	1	23	26
2	28	34	2	26	33
3	28	34	3	31	38
4	34	40	4	30	34
5	28	35	5	31	37
Average	28 minutes	34 minutes	Average	28 minutes	34 minutes
Heterogeneous wettability (1 glass 2 Teflon)			**Homogenous hydrophobic (0 glass 3 Teflon)**		
Trial	Liquid Island Formation (minutes)	Evaporation (minutes)	Trial	Liquid Island Formation (minutes)	Evaporation (minutes)
1	26	31	1	27	32
2	35	42	2	35	41
3	36	41	3	36	41
4	36	42	4	41	47
5	31	40	5	31	40
Average	33 minutes	39 minutes	Average	34 minutes	40 minutes

These results are consistent with the data from Chakraborty et al.[53] where their homogeneous hydrophobic simulated pore exhibited longer average evaporation times (42 minutes) compared to that of a homogeneous hydrophilic simulated pore (34 minutes). For the heterogeneous wettability cases, the evaporation times trended based on the predominant wettability (e.g., evaporation times for 2 glass, 1 Teflon were comparable to the homogeneous hydrophilic case); this result may be of use for applications in industry and agriculture, as less hydrophobic soil may lead to reduced runoff of water and better infiltration[4,5]. By integrating hydrophilic elements into predominantly hydrophobic soil, evaporation benefits may be obtained while also experiencing less runoff and better infiltration due to the soil being less hydrophobic.

Videos were analyzed in SolidWorks to plot the evolution of the projected length of contact (PLOC) and contact angles throughout evaporation; PLOC is used since the camera only captures a 2D view of the 3D pore. The data was procured by tracing the contact line from the top view and determining tangent lines to measure the contact angles in the side view. From there, utilizing the dimensions tool, the PLOC and contact angle measurements were determined. Contact angles were visualized using the side camera view and were measured at four points in the pore (Figure 2.1). These four points are the top and bottom visible edges of the contact line for the left and right bead.

On flat surfaces, Teflon and other hydrophobic media are associated with the CCA evaporative mode where droplets applied are generally depinned due to their contact angle of >90° and the movement of the triple contact line; likewise, glass and other hydrophilic media are associated with the CCR evaporative mode and generally being pinned[63]. However, in our experimental investigation with three spherical beads, this was not necessarily the case. For example, in the 2 glass 1 Teflon case (Figure 2.2b, 2.3b), water on the Teflon bead is pinned and exhibiting CCR evaporative mode through the first third of evaporation, whilst the glass bead has a moving contact line (i.e., depinning). This can be seen in the respective PLOC plot where the Teflon1 bead has a flat line through the first 10 minutes, indicating pinning, and the glass1 and glass2 beads have a slight negative slope, indicating depinning. Also, in the 1 glass 2 Teflon case (Figure 2.2c, 2.3c), all bead contact angles remain relatively constant for the first third of evaporation and then the "Left2" glass bead exhibits strong CCR indicated by a sharp negative slope in the graph while the Teflon bead "Right1" contact angle even increases, suggesting movement of the contact line. Generally, strong negative movement of the lines in the PLOC plots indicates depinning, with flatter lines indicating pinned contact lines. Within the contact angles plots, the reverse is true; strong negative movement of the lines indicates pinning, while flatter lines suggest depinning.

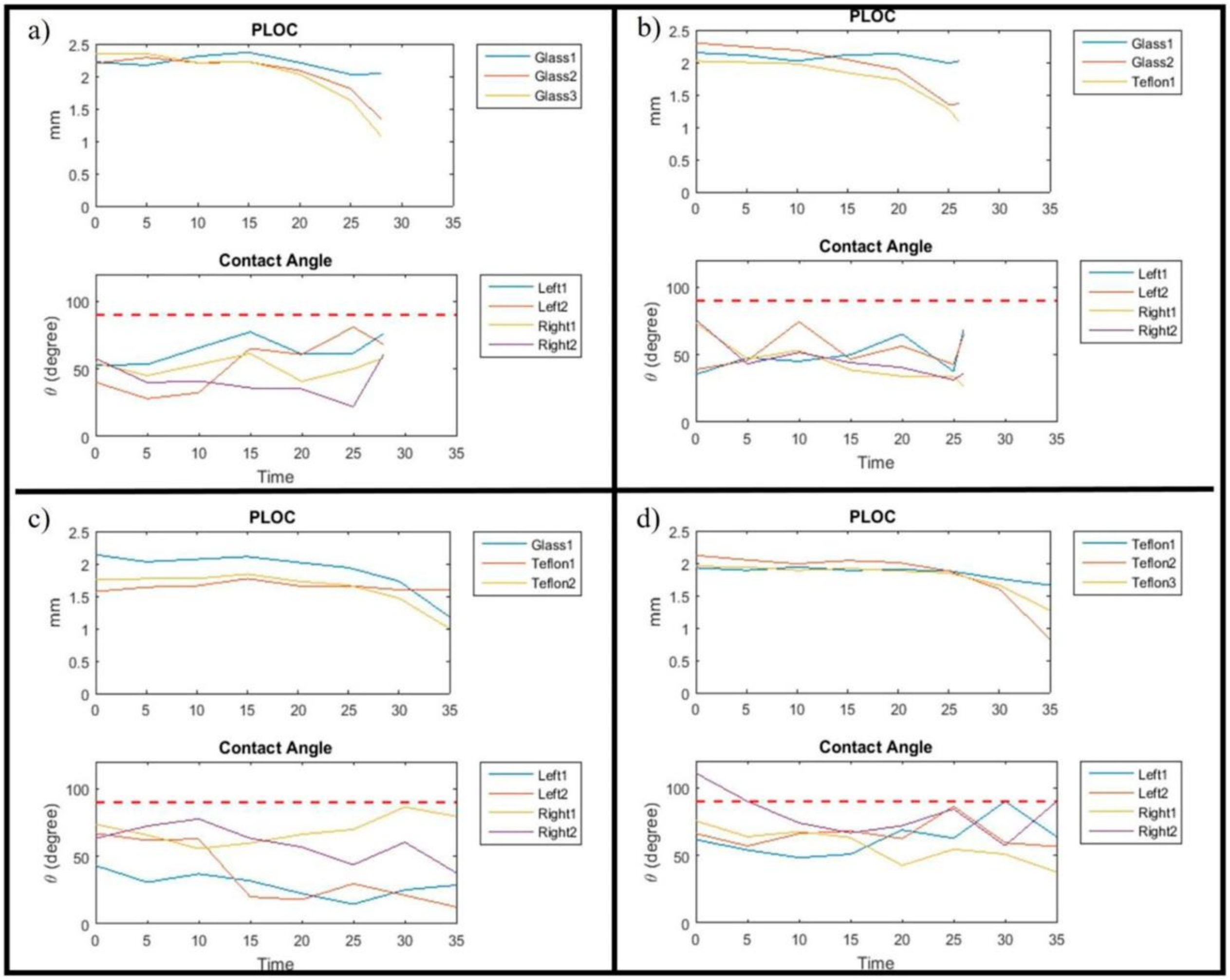

Figure 2.3: Projected length of contact and contact angle data throughout the evaporation time of all wettability arrangements. (a): 3 glass 0 Teflon. (b): 2 glass 1 Teflon. (c): 1 glass 2 Teflon. (d) 0 glass 3 Teflon[62]

This phenomenon where a mix of characteristic and uncharacteristic evaporative modes are observed is described by stick-slip theory[33], where a droplet can exhibit both modes intermittently or simultaneously to minimize the surface energy of the liquid droplet. As the droplet evaporates, it aims to maintain its intrinsic contact angle with a smoothly receding contact line, thereby minimizing the surface energy at an instant of time. However, this is prevented by pinning events corresponding to a previous equilibrium state. Referencing Eq. (1)[60] and applying it to the 1 glass

2 Teflon case (Figures 2.2c and 2.3c), we can gain insights into ongoing pinning/depinning dynamics. Eq. (1) was used by Orejon et al. for analysis on flat substrates, however, it is additionally useful for the analysis of curved interfaces. This is because the equation considers the triple contact line at the threshold of depinning, and the interfacial stresses can be modeled as in-plane stresses along the tangent planes of the curved surface at an instant of time[64]. Eq. (1) is applied to the beginning 15 minutes of this case due to the CCA mode throughout the first 10 minutes and then the sharp decrease in contact angle going into the 15th minute, corresponding to a stick-slip event. The "Left2" contact angle at the 10-minute mark is equal to 63° and at the 15-minute mark, which is the next measured time point, is 20°. From this time point on, the contact angle stays relatively constant for the duration of evaporation. Based on Eq. (1), depinning occurs when $\delta\theta$ is sufficiently large enough for $\delta\vec{F}$ to overcome the intrinsic energy barrier $\frac{\partial U}{\partial r}$. Between the 10- and 15-minute points, the "Left2" contact angle continually decreases until pinning forces are overcome and thus the triple contact line begins to move. So, for this case, $\delta\theta = 43°$ is a large enough difference to move the triple contact line. In another example, during evaporation in the 3 glass 0 Teflon arrangement (Figure 2.2a and 2.3a), the "Right2" contact angle at 0 minutes is 58° and at 5 minutes equals 40°, resulting in $\delta\theta = 18°$. It can be seen in the contact angle plot that after the 5-minute mark, the contact angle line is mostly flat, indicating movement of the contact line, sparked by the sufficiently large $\delta\theta$. In Figure 4, $\delta\vec{F}$ is plotted against $\delta\theta$ for numerous cases observed, showing the requirements for droplet depinning in their respective cases. Each data point shown in Figure 4 indicates a sufficiently large enough contact angle difference that sparked depinning. Ideally, there is no movement of the contact line until a sufficient contact angle difference is reached, which is indicated by the points that have been plotted. According to the data shown, various contact angle differences can produce depinning. Concurrently, the function

is plotted as a line for varying $\delta\theta$ in the example where $\theta_o = 90°$, which further shows the appositeness of applying Eq. (1) to curved surfaces as it is in good agreeance with our results.

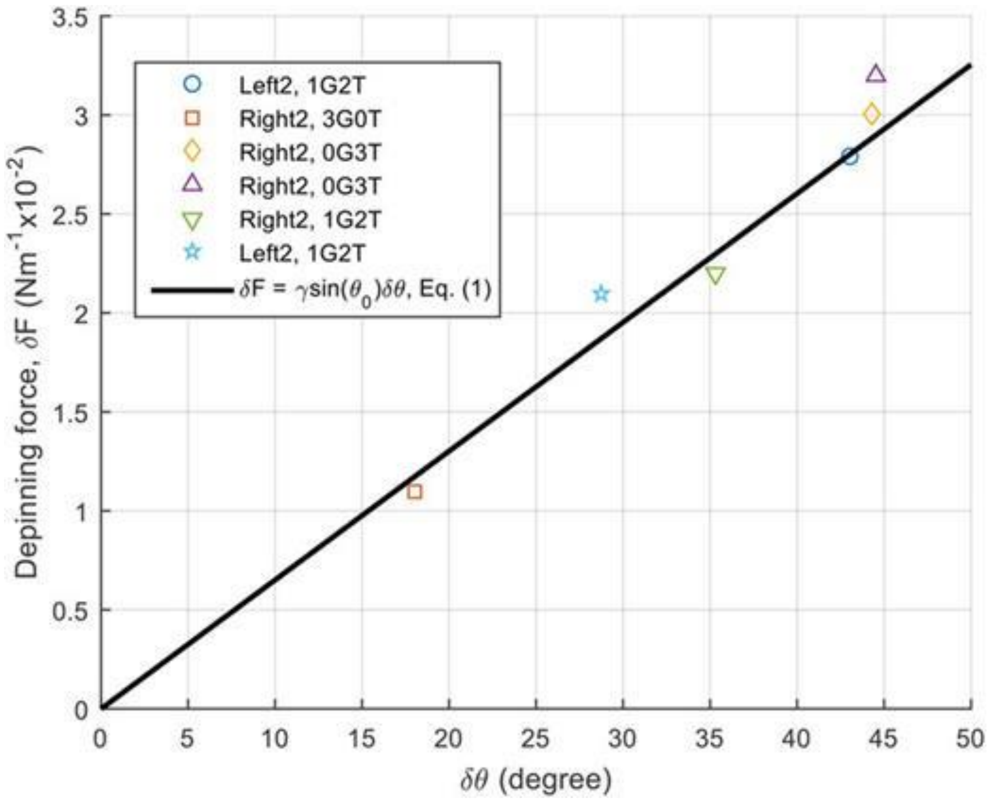

Figure 2.4: Sufficient depinning forces for numerous trials observed, plotted against $\boldsymbol{\delta\theta}$.[62] **Equation 1 is from Orejon et al.**[60]

Through all wettability arrangements considered, the stick-slip evaporative mode is observed, thereby suggesting that droplet pinning and depinning mechanics are also dependent on the geometry of the substrate[41,42]. Another instance of the stick-slip evaporative mode is seen in Figure 2.5 when considering the 2 glass 1 Teflon case (Figure 2.3b). Figure 2.5a shows the droplet upon initial placement and in Figure 2.5b, after 5 minutes has elapsed. The “Right 2” contact angle, indicated by a blue circle, decreases after the 5 minutes has elapsed, while remaining pinned. As this evaporation trial continued onward past the 5-minute mark, the “Right 2” contact angle remained fairly constant.

2.5a 2.5b

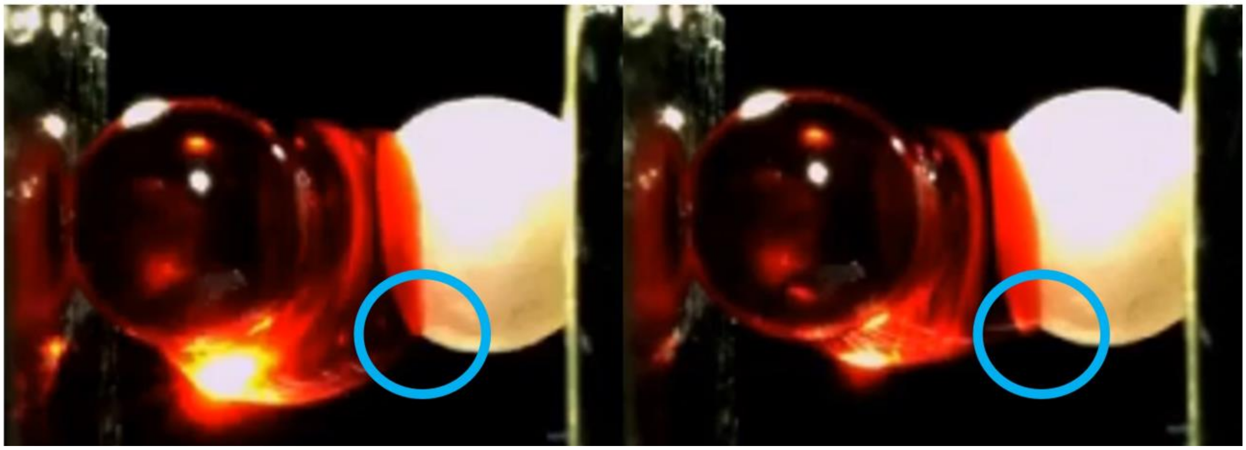

Figure 2.5: Visual difference in "Right 2" contact angle after 5 minutes for the 2 glass 1 Teflon configuration indicated by a blue circle. (a) Initial droplet placement. (b) Droplet after 5 minutes has elapsed.

Going from a 2D, flat surface to a 3D, curved, simulated soil pore creates an environment where hydrophilic media may appear with characteristics of hydrophobic media, and vice versa for hydrophobic media[65,66]. In one heterogeneous wettability (1 glass 2 Teflon; Figure 2.2c), the liquid island formed between the two Teflon beads rather than being formed between the glass and Teflon bead; it was expected that the liquid island would form between hydrophilic beads[67]. It is possible that even though hydrophobic material interacts with the liquid water interface less strongly compared to hydrophilic material[68], through surface energy optimization and pinning/depinning events occurring during evaporation, a liquid island can form between more hydrophobic structures. In the other four trials of the 1 glass 2 Teflon experiments conducted, island formation occurred between the glass and Teflon beads.

Dynamic contact angles are observed during evaporation. In Figure 2.3, a red, dotted line is placed at 90° to act as a visual aid to differentiate between hydrophobic and hydrophilic media. On a flat surface, Teflon has a contact angle of around 108°, and glass has a contact angle of around 41°, yet the values of the contact angles measured in these experiments on curved, simulated soil pores are often not near the reported values of 108° and 41°. For example, in the homogeneous hydrophobic (0 glass 3 Teflon) case, contact angles of 108° are achieved upon initial droplet placement, but also throughout the experiment, contact angles as low as 38° occur. A similar trend is often seen with the glass hydrophilic media in these experiments. Glass has a contact angle of around 41° on flat surfaces but contact angles on the glass bead are observed as low as 15° in the heterogeneous wettability (1 glass 2 Teflon) case and as high as 81° in the homogeneous hydrophilic (3 glass 0 Teflon) case. This is in contrast to the observations of Viswanadam and Chase[69] and Wu et al.[70] which noted that apparent contact angles of Teflon increased when placed onto a curved surface compared to that of a flat surface. These studies[69,70] examined a water droplet placed on top of a single solid sphere, and this paper's water droplet enters the middle of a simulated pore comprised of three spheres.

Although a key indicator, contact angle alone does not provide a complete description of the apparent wettability of a porous medium under intermediate-wet conditions[71]. The difference between the contact angles observed to the characteristic contact angles of the flat surface is likely due to the effects of pore geometry[72] and the motion of the droplet during evaporation, where Nabizadeh et. al[73] also noted a discrepancy between static equilibrium contact angles and dynamic contact angles recorded in their capillary tubes of varying geometries. Pore geometry exerts a fundamental influence on the apparent wettability of porous media due to the capillary pressure[72]

$$p_c = \gamma\kappa \tag{2.2}$$

Where $\boldsymbol{\kappa}$ is the curvature of the interface and $\boldsymbol{\gamma}$ is the surface tension at the interface. The capillary pressure will be different for the geometry considered by Viswanadam and Chase[69] and Wu et al.[70] compared to this work's geometry, inside of a simulated pore. This capillary pressure leads to distortions in the contact angle displayed, resulting in a possible explanation for the phenomena of contact angles differing from what is typically expected.

2.5 Conclusions

This work investigated the impacts of wettability on evaporation dynamics within simulated soil pores, specifically focusing on both homogeneous and heterogeneous wettability configurations. A 10-µL liquid droplet was placed into a three-dimensional simulated soil pore comprised of beads with varying wettability. Quantitative results indicate that homogeneous hydrophilic configurations exhibit the shortest average evaporation times at 34 minutes, while homogenous hydrophobic configurations display the longest, 40 minutes. However, the heterogeneous hydrophobic setup had average evaporation times of 39 minutes, indicating possible applications of altered wettability in agricultural settings to reduce runoff and increase infiltration while reducing evaporation. The stick-slip evaporative mode was observed, where droplets displayed CCA and CCR modes intermittently during evaporation. In some instances, hydrophobic Teflon beads displayed apparent contact angles indicative of hydrophilic media and vice versa for hydrophilic glass beads. Depinning forces were calculated for overcoming the intrinsic energy barrier during stick-slip evaporation. This research contributes valuable insights into soil pore evaporation mechanics, with implications for water conservation and agricultural practices in regions, such as the Ogallala Aquifer, facing significant water depletion challenges.

Chapter 3 - Utilization of Nuclear Microreactor Process Heat for Bioconversion and Agricultural Processes

3.1 Introduction

Nuclear microreactors are a subset of small modular reactors (SMRs), which are advanced nuclear reactors that produce electricity up to 300 MW_e per module[74]. Microreactors, however, typically have a power output of below 20 MW_e, but span a range from 1-50 MW_e[75]; specifications are tabulated in Table 1. Along with being carbon neutral, the small size and relative ease of deployment make microreactors excellent candidates for supplying power to military installations, remote areas, mining sites, and critical infrastructures such as hospitals[76]. They are valuable for use in remote or critical areas since microreactors are not limited by the need for continuous refueling, unlike diesel generators or small gas turbines. They can function within an electrical grid, independently, or contribute to a microgrid generating electricity and process heat. Currently, the main drawback of installing nuclear microreactors is their rate of return on investment, which is driven by high expected initial capital costs[77].

3.2 Research Objectives

The objective of this chapter is to serve as a guide for feasible bioconversion methods using the process heat of nuclear microreactor designs currently in development. Additionally, the research aims to provide a brief literature review of bioconversion and agricultural processes, focusing on their respective required operating conditions and parameters needed to interface with microreactors. To improve on their return on investment, research is being conducted to maximize the utility of the process heat created by microreactors[78]. One example, and a focus of this research, is the utilization of microreactor process heat for bioconversion methods such as gasification, pyrolysis, hydrothermal carbonization (HTC), hydrothermal liquefaction (HTL), and hydrothermal gasification (HTG). These bioconversion methods transform renewable biomass or organic materials into useful energy carriers or other valuable products, most notably, biofuels. Another focus of this work is the application of microreactor process heat for various agricultural processes, including ethanol production, anaerobic digester systems (AD), and pasteurization of milk.

3.3 Literature Review

This literature review focuses on the current microreactor technology available. The list of microreactor designs discussed is by no means exhaustive, however, the designs mentioned currently have the most publicly available information. Table 1 lists microreactor concepts along with their design features, power production, process heat availability, and operational conditions. The Xe-Mobile reactor, developed by X-energy, is a high-temperature, helium-cooled reactor design. It is capable of producing 1-5 MWe, fits in a standard shipping container, and can run at full power for at least three years[79,80]. Westinghouse has their own microreactor design, eVinci. This heat pipe fast neutron reactor design produces 5MWe, 13MWth, and is fully factory-built and fueled. These units can be set up in under 30 days and process heat up to 600℃ is available[6]. Oklo Inc. is a California-based company developing a 1.5MWe, 4MWth heat pipe fast nuclear microreactor known as Aurora[81,82]. The working fluid for the power conversion system, supercritical CO_2, has a maximum temperature of <550°C[82]. HolosGen is developing the Holos-Quad microreactor system in collaboration with the US military boasting a power output of 10MWe, 22MWth[83]. The design is that of a helium-cooled, high-temperature reactor with an average inlet/outlet coolant temperature of 590/850°C[84]. The Urenco U-Battery is a high-temperature reactor design with a 4 MWe power output[85]. The reactor would use TRISO fuel with

17-20% enriched uranium and possibly thorium with a beryllium oxide reflector. The U-Battery has process heat temperatures available up to 710°C and additional capabilities of pairing up to six U-Batteries at one site[86]. Finally, the MMR (Micro Modular Reactor) created by Ultra Safe Nuclear Corporation is another helium-cooled, high-temperature reactor design. The standard 2-unit MMR Energy System has a footprint of under 5 acres and employs minimal-impact civil construction techniques. Additionally, according to their official website regarding potential process heat applications, "steam temperatures of 660°C are simple[87]."

Table 3.1: Microreactor designs along with their respective features and operating conditions.

MICROREACTOR	TYPE	POWER	PROCESS HEAT
Xe-Mobile	High-temperature reactor (HTR), helium-cooled	1-5 MWe[79]	N/A
eVinci	Heat pipe fast neutron reactor (FNR)	5 MWe, 13MWth[6]	600°C process heat available[80,88]
Oklo Aurora	Heat pipe FNR	1.5 MWe, 4 MWth[81,82]	Maximum sCO2 working fluid temperature <550°C[82]
Holos-Quad	HTR, helium-cooled	10 MWe, 22 MWth[83]	Average inlet/outlet coolant temperature is 590/850°C[84]
U-Battery	HTR	4 MWe[86]	710°C process heat[86]
MMR (Micro Modular Reactor)	HTR, helium-cooled	3.5-15 MWe[87]	"Steam temperatures of 660°C are simple"[87]

It is important to note that a couple of these microreactor designs (i.e., Okla Aurora microreactor and Urenco U-Battery) are limited in their development. The Oklo Aurora microreactor's combined license application was denied by the U.S Nuclear Regulatory Commission, citing Oklo's failure to provide sufficient data on several crucial topics, while the U-battery failed to secure the commitment of key investors[89,90]. As Table 1 outlines, a sizable variety of microreactor design technology is available such as high-temperature gas reactors, light-water reactors, liquid metal fast reactors, molten salt reactors, and heat pipe reactors. As these microreactor designs operate based on distinct technologies, it leads to variations in the available process heat temperatures and therefore suitable applications.

As nuclear microreactors are a developing technology, it is important to establish strict safety measures and protocols. New customers looking to utilize microreactors may be unfamiliar or hesitant when dealing with nuclear fuel sources. When considering using microreactor process heat for concurrent operations, safety standards should remain high, and will likely need to see the convergence of industry and nuclear safety approaches. In short, when combining these two technologies, it is essential to conduct a thorough safety analysis that accounts for the individual safety protocols of each industry and any possible interactions between them. Notably, any event involving an abrupt energy release from one facility could have repercussions for the other.

3.4 Bioconversion and Agricultural Processes

Biomass feedstocks contributed approximately 1.3% to the total U.S. utility-scale electricity generation and made up 5.9% of electricity generation from renewable sources in 2022[91]. Electrical generation from all renewable energy sources globally is forecasted to increase from 29.5% in 2022 to 42% in 2028[92]. Nuclear microreactors could be leveraged for their process heat to facilitate bioconversion methods, and can also benefit agricultural processes. The processes described in this section are gasification, pyrolysis, HTC, HTL, HTG, ethanol production, AD systems, and pasteurization. This section briefly describes each process while highlighting operating conditions.

3.4.1 Gasification

Gasification is a thermochemical process in which carbon-based fuels in sub-stoichiometric conditions are transformed into a combustible gas known as syngas (i.e., producer gas, product gas, synthetic gas, or synthesis gas), along with byproducts tar and char[93,94] This syngas is primarily composed of CO, H_2, CH_4, CO_2, water vapor, smaller amounts of H_2S, COS, and other trace contaminants[95]. However, the composition of the syngas greatly depends on the feedstock utilized. Ideally in gasification, the moisture in the biomass feedstock is below 30%. If this is not the case, the gasification efficiency significantly decreases due to some energy being spent towards vaporization, thereby decreasing the gasification temperature. The gasification temperature is preferably high, as less tar and char are produced at higher temperatures, resulting in a greater syngas yield. The carbonaceous biomass is treated at temperatures from 600 °C to 1200 °C and can be pressurized or unpressurized with air as a working fluid[96]. Pressurized gasifiers may be useful when coupled with a turbine for concurrent electrical generation; however, they are more complex and bring high operational costs[97].

3.4.2 Pyrolysis

Pyrolysis is a similar thermochemical process to gasification in which the main differences are the lack of a gasifying agent and a lower process temperature[98] The biomass feedstock is thermally degraded in an inert environment, resulting in the production of bio-oil, biochar, and syngas[99]. The proportions of these products greatly depend on the feedstock used and the operating parameters. Like gasification, the feedstock should have a low moisture content to avoid preliminary drying. There are three types of pyrolysis: slow pyrolysis, fast pyrolysis, and flash pyrolysis, which vary in their process temperature and residence times. Slow pyrolysis operates at 300 °C to 550 °C, with a residence time of 5-30 minutes and a heating value of 10 °C/min. Fast pyrolysis operates at 500 °C to 600 °C, with a residence time of 0.5-2 seconds and a heating value of 10-1000 °C/s. Flash pyrolysis operates at 900 °C to 1300 °C, with a residence time of less than 0.5 seconds and a heating value of greater than 1000 °C/s[100]. Bio-oil production is maximized at process temperatures of 500 °C and a heating rate of 1000 °C/s, where bio-oil yields can reach 60-70 wt% from a typical biomass feedstock[101].

3.4.3 Hydrothermal Carbonization

Unlike gasification and pyrolysis, hydrothermal carbonization (HTC) requires significantly lower process temperatures in the range of 180 °C to 350 °C[102]. During hydrothermal carbonization, the goal is the combined dehydration and decarboxylation of the biomass feedstock to achieve a higher calorific value[103]. Along with a gas fraction and an aqueous liquid fraction, this results in the end product being a lignite-like char called hydrochar. Hydrothermal carbonization is conducted in pressurized water. Being that the process is wet, this negates the need for feedstocks to reach a certain moisture level, thereby enabling a larger variety of feedstocks to be utilized. The pressure required for hydrothermal carbonization is determined by the saturation pressure of water at the process temperature (i.e., autogenous pressure), typically between 2 to 10 MPa[98]. Common feedstocks for hydrothermal carbonizations are rich in cellulose and include bagasse, straw, corn, and stover[104].

3.4.4 Hydrothermal Liquefaction

Hydrothermal liquefaction (HTL) is similar to hydrothermal carbonization in that the process is carried out in a wet environment, thereby enabling the treatment of wet biomass. Rather than the production of a hydrochar, hydrothermal liquefaction produces bio-oil, with aqueous phase products, gas phase products, and solid residues as byproducts[105]. The process is run at slightly more elevated temperatures [i.e., 250 °C to 375 °C[106]]. Hydrothermal liquefaction is also run at autogenous pressures, usually in the range of 5 to 20 MPa; these pressures are higher due to the increased operating temperatures associated with the process[107]. In the hydrothermal liquefaction process, biomass macromolecules undergo initial hydrolysis and/or degradation, resulting in the formation of smaller molecules. A significant portion of these newly formed molecules are characterized by instability and reactivity, leading to their combination into larger molecules. Throughout this transformation, a considerable amount of oxygen within the biomass is eliminated through dehydration or decarboxylation[108]. As with all of the bioconversion methods mentioned, the chemical attributes of the manufactured bio-oil exhibit a strong reliance on the composition of the feedstock utilized[109].

3.4.5 Hydrothermal Gasification

Hydrothermal gasification (HTG), also referred to as supercritical water gasification, is akin to both hydrothermal carbonization and liquefaction in that it takes place in a wet environment. However, hydrothermal gasification is a bioconversion method that seeks to produce fuel gas/syngas instead of solid or liquid fuel. The process involves the hydrolysis of biomass in supercritical water followed by further gasification of the produced aqueous oligomers[110]. The reaction time is short, making it one of the most efficient technologies for wet biomass gasification. The operating temperatures and pressures associated with this process are 350 °C to 700 °C and 21 to 30 MPa[100,111]. Similar to other processes, the composition of the syngas is heavily dependent on the feedstock. It is also important to note, according to the Le Chatelier principle, that hydrogen formation is preferred at high temperatures, while methane formation is more suited to higher pressures[112]. This flexibility in product output could be a significant factor for manufacturers.

3.4.6 Ethanol

Ethanol production is a key bioconversion process with substantial implications for renewable energy and sustainable practices. Ethanol, a widely available biofuel, can be used as an alternative to traditional fossil fuels. Ethanol is typically produced through the fermentation of sugars derived from biomass, such as sugarcane, corn, or lignocellulosic materials[113]. The efficiency of this process is influenced by factors such as feedstock composition, fermentation conditions, and the choice of microorganisms, such as yeast[114]. Compared to the previously mentioned techniques, the fermentation process for maximum ethanol production requires very moderate temperatures, typically between 30 °C and 35 °C. However, during the pretreatment steps before fermentation, the highest operational temperatures may be found, reaching as high as 240 °C[115]. These temperatures are needed when hydrolyzing holocellulose using dilute acids.

3.4.7 Anaerobic Digestion

Anaerobic digestion (AD) is a biological process where anaerobic consortia including methanogenic archaea convert organic waste into carbon dioxide and methane (i.e., biogas)[116]. Anaerobic treatment offers a means to diminish pollution arising from agricultural and industrial activities, while simultaneously mitigating their reliance on fossil fuels. The efficiency of anaerobic digestion is influenced by several factors, including the composition of the organic waste, process temperature, retention time, and the microbial community involved[117]. The microbial community driving anaerobic digestion prefers mesophilic conditions, exhibiting accelerated growth within the temperature range of 25 °C to 40 °C, but when temperatures exceed 47 °C, these methanogens die[118]. In the absence of these methanogens, alternate microbial communities assume control of methane production in the thermophilic state (40 °C to 55 °C), where the rate of methane production is lower. The overall gas pressure within a typical anaerobic digester is kept slightly higher than atmospheric pressure, with an overpressure of up to 0.02 bar[119].

3.4.8 Pasteurization

Pasteurization is a key agricultural process, particularly in the dairy industry. Conventional pasteurization processes rely on continuous heat transfer to eliminate harmful pathogenic organisms in liquids like milk and slightly extend product shelf life[120]. The most common means of heating comes from the use of plate heat exchangers due to their low cost, flexibility, high thermal efficiency, and ease of maintenance. For the pasteurization of milk, there are two common techniques: batch pasteurization and continuous flow pasteurization. In batch pasteurization, milk in a large vat or tank is heated to at least 63 °C for a minimum of 30 minutes. Continuous flow pasteurization methods include high-temperature, short-time (HTST) pasteurization, which heats milk to a minimum of 72 °C for 15 seconds, and ultra-high temperature (UHT) pasteurization, employing temperatures ranging from 135 °C to 150 °C for 4-15 seconds[121].

3.5 Brayton Cycle Model

To understand how these bioconversion and agricultural processes may be integrated with nuclear microreactor heat, a Brayton cycle model was developed. The model presented is based on published information about the Westinghouse eVinci microreactor. The eVinci microreactor can produce 5 MW_e with a 13 MW_{th} design. The eVinci microreactor uses heat pipe cooling technology, with the power conversion system being an open-air Brayton cycle with an approximate efficiency of 36%[122]. Because of this available information concerning the eVinci power conversion system, this design was chosen over other microreactors which currently have less available design information. To realize this 36% cycle efficiency, a regenerator is incorporated into the model (Figure 3.1). An additional, second heat exchanger (HTX) has been added to the cycle to accommodate the bioconversion/agricultural processes; the dotted boxes in Figure 3.1 indicate the potential positions for HTX.

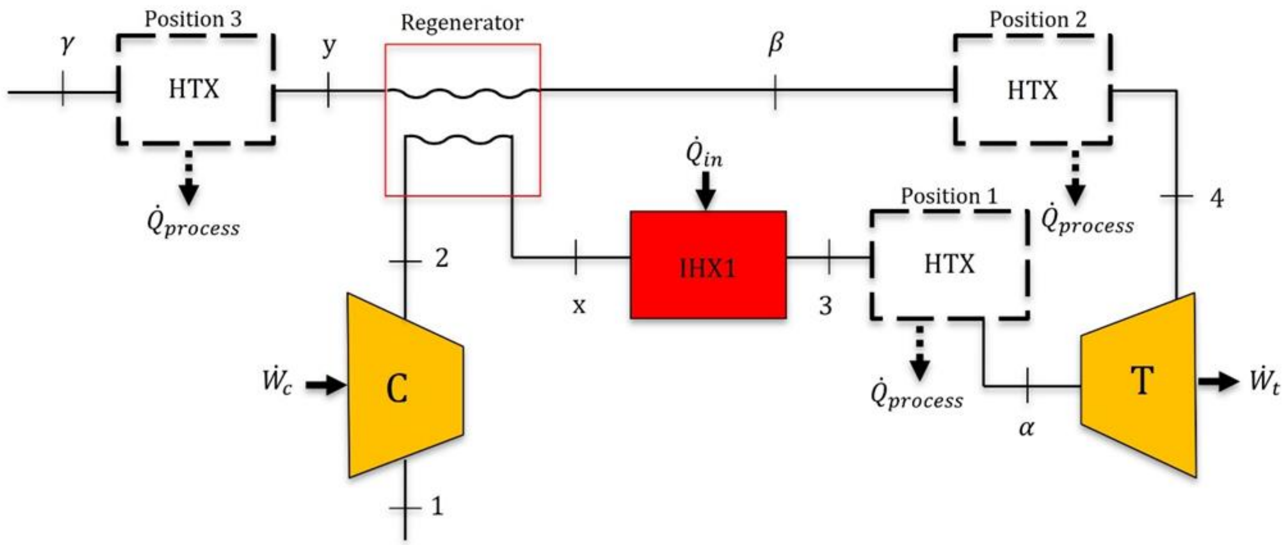

Figure 3.1: Representative regenerative Brayton cycle diagram including an additional heat exchanger (HTX) shown in three possible positions for supplying heat to the concurrent processes, depicted by dotted boxes.

The primary equations needed to build this model in EES are presented here. For the compressor,

$$\eta_c = \frac{h_{2s} - h_1}{h_2 - h_1} \tag{3.1}$$

where η_c is the compressor isentropic efficiency, h_{2s} is the isentropic-specific enthalpy at state 2, h_1 is the specific enthalpy at state 1, and h_2 is the specific enthalpy at state 2. For the turbine,

$$\eta_t = \frac{h_\alpha - h_4}{h_\alpha - h_{4s}} \tag{3.2}$$

where η_t is the turbine isentropic efficiency, h_{4s} is the isentropic-specific enthalpy at state 4, h_α is the specific enthalpy at state α, and h_4 is the specific enthalpy at state 4. For the regenerator,

$$\varepsilon_{reg} = \frac{h_x - h_2}{h_\beta - h_2} \tag{3.3}$$

where ε_{reg} is the regenerator effectiveness, h_x is the specific enthalpy at state x and h_β is the specific enthalpy at state β. The mass flow rate of the air is determined using an energy balance,

$$\dot{m}_a = \frac{\dot{Q}_{in}}{h_3 - h_x} \tag{3.4}$$

where $\dot{m}_a$ is the mass flow rate of air in the Brayton cycle, $\dot{Q}_{in}$ is the heat supplied by the microreactor, and h_3 is the specific enthalpy at state 3. Applying an energy balance to the regenerator yields

$$h_y = h_2 + h_\beta - h_x \tag{3.5}$$

where h_y is the specific enthalpy at state *y*. The overall cycle thermal efficiency is,

$$\eta_{cycle} = \frac{(h_\alpha - h_4) - (h_2 - h_1)}{h_3 - h_x}. \tag{3.6}$$

In the HTX for position 1,

$$\dot{Q}_p = \dot{Q}_{out} = \dot{m}_a(h_3 - h_\alpha) \tag{3.7}$$

where $\dot{Q}_p$ is the heat used by the concurrent process and $\dot{Q}_{out}$ is the heat emitted by HTX. For position 2,

$$\dot{Q}_p = \dot{Q}_{out} = \dot{m}_a(h_4 - h_\beta) \tag{3.8}$$

where h_β is the specific enthalpy at state β. For position 3,

$$\dot{Q}_p = \dot{Q}_{out} = \dot{m}_a(h_y - h_\gamma) \tag{3.9}$$

where h_γ is the specific enthalpy at state γ. The process fluid mass flow rate is obtained using an energy balance,

$$\dot{m}_p = \frac{\dot{Q}_p}{h_p - h_a} \tag{3.10}$$

where $\dot{m}_p$ is the mass flow rate of the process working fluid, h_p is the specific enthalpy at state *p* and h_a is the specific enthalpy at state *a*. For the heat exchanger in position 1,

$$\varepsilon_{HTX,1} = \frac{C_c(T_p - T_a)}{C_{min}(T_3 - T_a)} = \frac{C_h(T_3 - T_\alpha)}{C_{min}(T_3 - T_a)} \tag{3.11}$$

where $\varepsilon_{HTX,1}$ is the effectiveness of HTX at position 1, C_c is the heat capacity rate of the cold flow, C_h is the heat capacity rate of the hot flow, C_{min} is the smaller heat capacity rate between C_c and C_h, T_p is the temperature at state p, T_a is the temperature at state a, and T_α is the temperature at state α. For the heat exchanger in position 2,

$$\varepsilon_{HTX,2} = \frac{C_c(T_p - T_a)}{C_{min}(T_4 - T_a)} = \frac{C_h(T_4 - T_\beta)}{C_{min}(T_4 - T_a)} \quad (3.12)$$

where T_β is the temperature at state β. For the heat exchanger in position 3,

$$\varepsilon_{HTX,3} = \frac{C_c(T_p - T_a)}{C_{min}(T_y - T_a)} = \frac{C_h(T_y - T_\gamma)}{C_{min}(T_y - T_a)} \quad (3.13)$$

where T_γ is the temperature at state γ. Overall net power production is based on

$$\dot{W}_{net} = \dot{m}_a[(h_\alpha - h_4) - (h_2 - h_1)] \quad (3.14)$$

where $\dot{W}_{net}$ is the net power done by the Brayton cycle.

The placement of the HTX is flexible, depending on the heat requirements of a given process. For processes requiring high temperatures, placing the HTX immediately before the turbine at position 1 may be optimal, as this is where the highest temperatures are available, yet that decreases the net power the cycle may produce. For processes that require lower temperatures, the HTX can be positioned between the turbine and the regenerator or after the regenerator. Assumptions for the Brayton cycle model include using an air standard analysis, state 1 having ambient conditions of 1 atm and a temperature of 20 °C, no pressure drop through the heat exchangers, a turbine isentropic efficiency of 92%[123], a compressor isentropic efficiency of 85%[123], and a regenerator effectiveness of 90%[124]. Corresponding to the eVinci Brayton cycle, $\dot{Q}_{in} = 13MW$, $\eta_{cycle} = 36\%$; the states were set using equations 3.1 through 3.5. Additionally, assumptions have been made about the working fluid for each process due to different working fluids having different specific heats, c_p. For AD, ethanol production, HTC, HTL, and HTG, water was used as the working fluid[98,115,125]. Milk was assumed the working fluid for pasteurization, air was used for gasification[96], and nitrogen was used for pyrolysis[126].

3.6 Results and Discussion

3.6.1 Exergetic Efficiency

In order to assess the feasibility of coupling bioconversion and agricultural methods with nuclear microreactors, exergetic (second law) efficiencies are computed, and power and heat tradeoffs are calculated for different processes. Exergetic efficiency is useful when matching an end use to a source and it is given by

$$\varepsilon = \eta \left(\frac{1-T_0/T_u}{1-T_0/T_s}\right), \text{ with } \eta = \frac{\dot{Q}_u}{\dot{Q}_s} \tag{3.15}$$

where ε is the exergetic efficiency, T_0 is the ambient temperature, T_u is the use temperature, T_s is the source temperature, η is an efficiency in terms of energy rates, $\dot{Q}_u$ is the heat transfer rate available for use, and $\dot{Q}_s$ is the heat transfer rate delivered into the system from the fuel source. In the ideal case, $\eta = 1$. When a source temperature is significantly greater than what is required for a certain task, the end use leads to inefficiencies [127]. In Table 3.2, the exergetic efficiencies at position 1 (i.e., before the turbine) for different microreactor designs, coupled with the different bioconversion and agricultural process, are shown; N/A indicates an exergetic efficiency of greater than 100%, which is impossible.

Table 3.2: Exergetic efficiency values for different microreactor designs at position 1(i.e., before the turbine) when coupled with bioconversion and agricultural processes. T_s is the microreactor source temperature given in Table 1 and T_u is the temperature range or value for each process. "N/A" is for the cases where the source temperature is lower than the use temperature, leading to exergetic efficiencies greater than 100%. Red indicates $75\% \leq \varepsilon \leq 100\%$, light red indicates $50\% \leq \varepsilon < 75\%$, blue indicates $25\% \leq \varepsilon < 50\%$, light blue indicates $0\% \leq \varepsilon < 25\%$, and black is for N/A (>100%).

EXERGETIC EFFICIENCIES	Holos-Quad, $T_s =$ 850℃	U-Battery, $T_s =$ 710℃	MMR, $T_s =$ 660℃	E-Vinci, $T_s =$ 600℃	Oklo Aurora, $T_s =$ 550℃	SEALER, $T_s =$ 420℃
Gasification, $T_u =$ 600℃ – 900℃ [98]	90% - N/A	95% - N/A	97% - N/A			
Hydrothermal Gasification, T_u = 350℃ – 700℃ [100]	72% - 95%	75% - 100%	77% - N/A	80% - N/A	82% - N/A	92% - N/A
Pyrolysis, T_u = 500℃ [101]	84%	88%	91%	93%	96%	
Hydrothermal Liquefaction, T_u = 250℃ – 375℃ [106]	60% - 74%	63% - 78%	64% - 80%	66% - 82%	68% - 85%	76% - 95%
Hydrothermal Carbonization, T_u = 180℃ – 350℃ [102]	49% - 72%	50% - 75%	52% - 77%	53% - 80%	55% - 82%	61% - 92%
Ethanol, T_u = 240℃ [115]	58%	61%	63%	65%	67%	75%
Pasteurization, T_u = 63℃ – 150℃ [121]	17% - 42%	18% - 44%	19% - 45%	19% - 46%	20% - 48%	22% - 53%
Anaerobic Digestion, T_u = 25℃ – 40℃ [118]	2% - 9%	2% - 9%	3% - 9%	3% - 10%	3% - 10%	3% - 11%

These results indicate that some of the high-temperature processes, like gasification and pyrolysis, are well-matched to the source temperatures. Although the exergetic efficiencies are high, there are significant tradeoffs when considering the power generated in the cycle. Larger amounts of heat are required for the bioconversion processes, thereby diminishing the power produced by the turbine. For microreactor designs with lower reported process heat temperatures, processes such as hydrothermal carbonization, hydrothermal liquefaction, and ethanol production are well-suited. Low-temperature processes like pasteurization and anaerobic digestion have the lowest exergetic efficiency percentages and are better suited for using lower-grade waste heat (e.g., position 2 or 3 in Figure 3.1). It is also noteworthy that these exergetic efficiency values have been calculated for the case in which only a singular process is being integrated into the microreactor; it may be possible to run more than one process. Another consideration is that these exergetic efficiency results have been calculated at the peak process temperatures provided by each microreactor. In the next section of results, the differences in process heat at different locations within the Brayton cycle model are investigated.

3.6.2 Tradeoffs Between Process Heat Utilization and Power Production

Next, this chapter focuses on the heat and power tradeoffs when meeting the temperature requirements of the bioconversion and agricultural processes. To achieve this, the model in EES calculated the net cycle work and maximum rate of heat transfer from the HTX when placed at three different potential locations (Figure 3.2). The numerical results from these calculations are available within Tables 3.3, 3.4, and 3.5. The process temperatures used are the average temperature values for each process (Section 3.4 and Table 3.2) As Figure 3.2 demonstrates, different processes are omitted for different HTX positions due to their incompatibility (e.g., negative amounts of $\dot{W}_{net}$ produced due to the process requiring large amounts of $\dot{Q}_{process}$ or when the cycle had temperatures lower than the process required).

Table 3.3: Brayton cycle model outputs for HTX position 1 (i.e., before the turbine).

Position 1	T_p [K]	$\varepsilon_{HTX,1}$	$\dot{Q}_p$ [kW]	$\dot{W}_{net}$ [kW]	$c_{p,c}$ [J/gK]	Process Fluid
AD	313.2	0.07045	511	4423	4.179	Water
Pasteurization	423.2	0.4415	2973	3183	3.94	Milk
Ethanol	513.2	0.7367	4238	2544	4.754	Water

HTC	538.2	0.8546	4508	2407	5.035	Water
HTL	585.7	0.9028	4828	2245	6.014	Water
Pyrolysis	773.2	0.8361	10905	-872.6 (not possible)	1.116	Nitrogen
HTG	798.2	0.9521	8375	438.7	3.489	Water
Gasification	873.2	1	11845	-1363 (not possible)	1.115	Air

Table 3.4: EES parametric table outputs for HTC position 2 (i.e., between turbine and regenerator).

Position 2	T_p [K]	$\varepsilon_{HTX,1}$	$\dot{Q}_p$ [kW]	$\dot{W}_{net}$ [kW]	$c_{p,c}$ [J/gK]	Process Fluid
AD	313.2	0.1603	482.4	4524	4.179	Water
Pasteurization	423.2	0.3980	2707	3803	3.94	Milk
Ethanol	513.2	0.7878	3789	3453	4.754	Water
HTC	538.2	0.8991	4015	3379	5.035	Water
HTL	585.7	0.9134	4280	3293	6.014	Water

Table 3.5: EES parametric table outputs for HTX position 3 (i.e., after the regenerator).

Position 3	T_p [K]	$\varepsilon_{HTX,1}$	$\dot{Q}_p$ [kW]	$\dot{W}_{net}$ [kW]	$c_{p,c}$ [J/gK]	Process Fluid
AD	313.2	0.1954	490.2	4680	4.179	Water
Pasteurization	423.2	0.4438	3275	4680	3.94	Milk

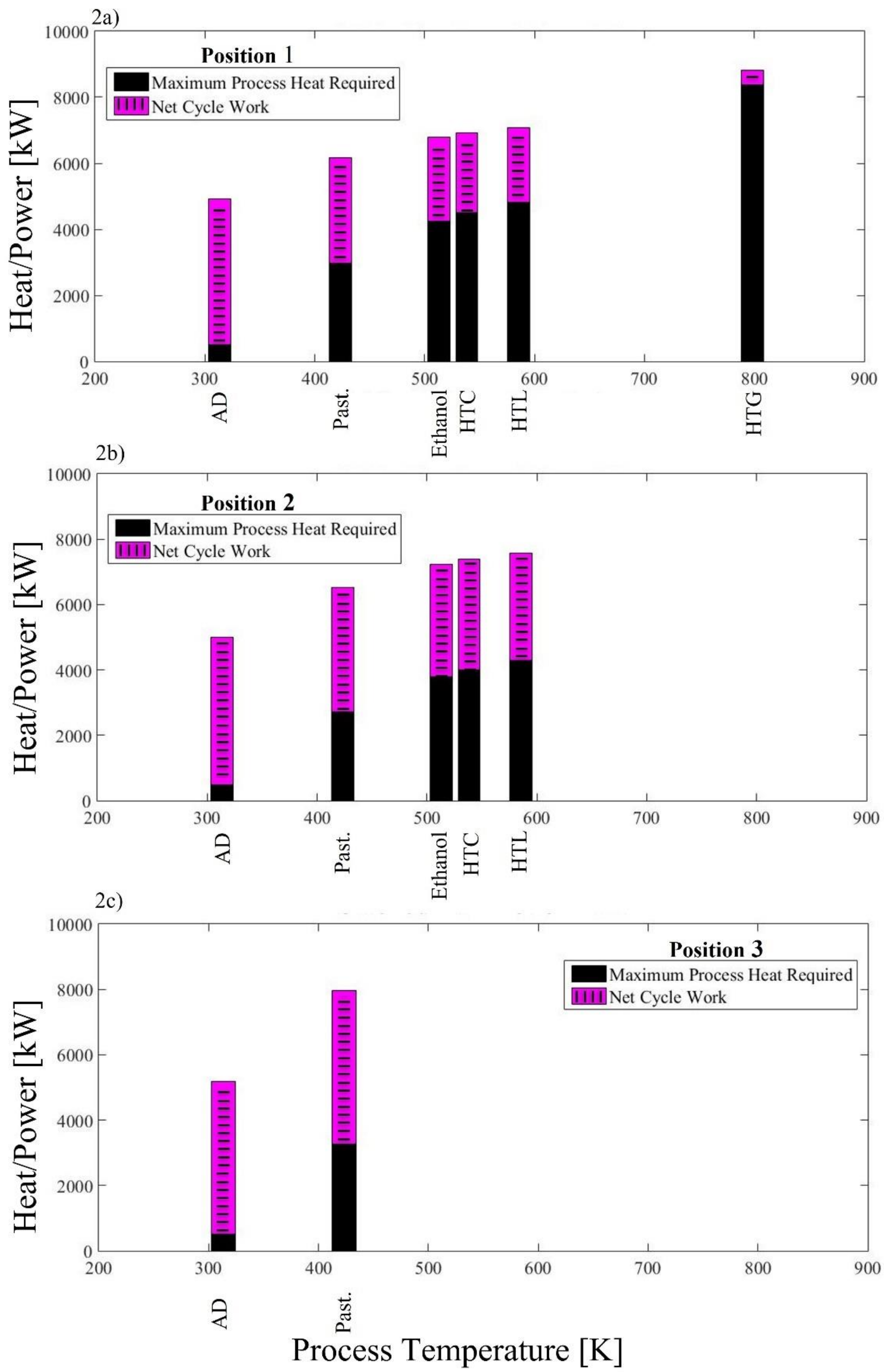

Figure 3.2: Power and maximum process heat tradeoff plots when HTX is placed at three different locations: 3.2a) position 1, between the turbine and IHX1, 3.2b) position 2, between the turbine and regenerator, and 3.2c) position 3, after the regenerator. Acronyms used: HTC (Hydrothermal carbonization), HTL (Hydrothermal liquefaction), HTG (Hydrothermal gasification), AD (Anaerobic digestion), Past. (Pasteurization).

In Figure 3.2a, where the HTX is placed ahead of the turbine and has access to the highest temperatures in the cycle (i.e., position 1), all the processes are viable besides gasification and pyrolysis, as according to the model these will bring the inlet turbine temperature too low to result in a positive $\dot{W}_{net}$. As process temperatures increase, larger amounts of maximum process heat are needed, thereby decreasing the net power produced in the cycle. Although pyrolysis necessitates lower temperatures than HTG, due to HTG using a superior heat transfer fluid (water), it is the highest temperature process available for a positive cycle efficiency; pyrolysis and gasification resulted in negative amounts of $\dot{W}_{net}$, and, therefore, are excluded.

For position 2, (i.e., between the turbine and regenerator; Figure 3.2b), the available process temperatures in the Brayton cycle are lower than position 1, at around 643 K. In this position, pyrolysis and HTG are eliminated as their process temperature requirements are greater than 643 K. Ethanol production, HTC, and HTL are still viable and strike a balance between running a concurrent process while also having sizable net power.

Finally, in position 3 (i.e., after the regenerator), depicted in Figure 3.2c), the lowest process temperatures are available at 465 K. At this process temperature, only AD and pasteurization are viable. However, since position 3 is when HTX is after the regenerator, $\dot{W}_{net}$ is not affected. This can be interpreted as the excess heat for position 3 being free waste heat, since the change in $\dot{Q}_{process}$ does not interfere with $\dot{W}_{net}$. As briefly mentioned earlier, this model considers powering only a single process at a time and examining how this affects cycle efficiency. The results from this model show that there are tradeoffs when considering the positioning of a heat exchanger for bioconversion and agricultural processes, where certain processes are more optimal. If investors and consumers are more interested in the concurrent processes, and less so in electrical power generation, matching processes could be tailored with these interests in mind and vice versa.

3.7 Conclusions

Addressing the pressing issue of global warming requires a multifaceted approach where the utilization of nuclear microreactors may play a significant role. In this brief research report, the feasibility of using nuclear microreactors for concurrent bioconversion and agricultural processes was investigated. Exergetic efficiency results of 72-100% showed high compatibility between high-temperature processes (i.e., gasification, HTG, and pyrolysis) at position 1, while lower temperature processes (i.e., AD and pasteurization) with exergetic efficiencies of 2-53% could result in some of the microreactor heat being utilized less efficiently from an exergetic viewpoint. A Brayton cycle model with a regenerator was developed to assess the feasibility of powering these processes using nuclear microreactor heat. From this model, power and heat tradeoff analyses were studied to provide insights into the feasibility of utilizing excess heat for different processes. Results indicated that high-temperature techniques such as gasification, requiring a minimum of 600℃, are impractical within the model due to excessive heat demands. Position 1, situated before the turbine, yielded the highest process temperatures at 600℃, followed by position 2 at 370℃, and position 3 at 192℃. Certain processes, such as ethanol production, HTC, and HTL, are better suited for position 2, positioned between the turbine and regenerator, although they can also operate at position 1. Conversely, lower temperature processes like pasteurization and AD can utilize waste heat at position 3 after the regenerator, thus having no impact on power production.

Chapter 4 - Conclusions and Future Work

In this thesis, two crucial aspects of sustainable development within the context of the FEW (Food, Energy, and Water) nexus were examined: the impact of mixed wettability on evaporation dynamics for agricultural settings and the utilization of nuclear microreactor process heat for bioconversion and agricultural processes. Through this research, contributions have been made to uncover solutions that address pressing challenges facing humanity in the 21st century such as the depletion of the Ogallala Aquifer and addressing global carbon emissions.

In Chapter 2, the influence of mixed wettability on the evaporation dynamics of water droplets in simulated soil pores was investigated, shedding light on potential strategies for water conservation in agricultural systems. With this, it was demonstrated how variations in pore wettability can significantly affect evaporation rates and mechanisms. Consistent with prior literature[3,17,53], it was determined that hydrophobic arrangements demonstrate longer evaporation times compared to hydrophilic arrangements. Homogeneous hydrophilic configurations exhibited the shortest evaporation times of 34 minutes while homogeneous hydrophobic configurations were the longest at 40 minutes. The heterogeneous hydrophobic configuration had the second longest evaporation times at 39 minutes, pointing to possible applications where altered wettability soil can have benefits of both hydrophobic and hydrophilic soil. The stick-slip evaporative mode was observed in all wettability arrangements and in some instances, hydrophobic Teflon beads displayed hydrophilic contact angles and vice versa for the hydrophilic glass beads. These results suggest that targeted modifications of soil wettability could offer promising avenues for mitigating water loss and improving irrigation efficiency, thereby contributing to the resilience of agricultural ecosystems in the face of water scarcity challenges.

Chapter 3 focused on the feasibility of harnessing process heat from nuclear microreactors for various bioconversion and agricultural processes, aiming to advance carbon-neutral power generation and mitigate the emission of greenhouse gases. The exergetic efficiencies of different processes coupled with the microreactor model were determined, identifying optimal configurations for utilizing nuclear microreactor heat. Exergetic efficiencies of 72-100% indicate high compatibility between high temperature processes (i.e., gasification, HTG, and pyrolysis) at position 1. In contrast, lower temperature processes (i.e., AD and pasteurization) with exergetic efficiencies of 2-53% may result in less efficient utilization of microreactor heat from an exergetic perspective. Next, tradeoffs were considered between the net power production of the Brayton cycle model and the heat required for each process. Three distinct positions for the heat exchanger were evaluated. The findings indicate that processes requiring high temperatures, such as gasification (minimum 600℃), pose feasibility challenges according to our model. Among the options considered, the heat exchanger placed before the turbine yielded the highest process temperatures at 600℃, followed by the position between the turbine and regenerator (370℃), and finally, the location after the regenerator (192℃). Certain processes, such as ethanol production, hydrothermal carbonization, and hydrothermal liquefaction, are better suited for a heat exchanger situated between the turbine and the regenerator. However, they can also operate at position 1 before the turbine. Lower temperature processes like pasteurization and anaerobic digestion were found to effectively utilize waste heat after the regenerator, without compromising power production. These findings emphasize the importance of considering process integration and heat management strategies in the design and operation of nuclear microreactors to maximize their potential in supporting sustainable agricultural practices and fully utilize their potential.

By understanding these findings within the framework of the FEW nexus, the interconnectedness of food, energy, and water systems is further demonstrated. As we move forward into a more resilient and responsible future, it is imperative to recognize the complex interactions and trade-offs inherent in the management of the FEW nexus. The projects presented here are only a glimpse into the numerous aspects in which we can promote a healthier, more sustainable future under the umbrella of the FEW nexus.

Future work into mixed wettability systems may include further understanding of how pore geometry and capillary pressure influence dynamic contact angles, evaporation modes, and evaporation times. Additionally, future work could entail how changing certain aspects of this work's experimental setup affects evaporation dynamics. This could include changing the bead material to increase or decrease the difference in wettability between beads, increasing or decreasing the pore spacing, or introducing additional beads (scaling up). Since the end goal of this research is to mitigate water loss in agricultural and drought-prone settings, future work can be conducted to determine how to change wettability characteristics over large portions of land by considering a larger lab scale and, eventually entire, fields. As these larger scales are reached, insights into how wettability alterations decrease or increase water runoff should be considered.

Future work regarding nuclear microreactors holds promising avenues for research and development. Firstly, there is a need to optimize the integration of these processes with microreactors, focusing on maximizing overall system efficiency through further thermodynamic modeling and simulations. Currently, this can be challenging due to the information surrounding nuclear microreactors largely being proprietary and not publicly available in the published literature. Ideally, as nuclear microreactors draw further attention from larger governmental bodies, this information may be more readily accessible. Exploring the feasibility of integrating multiple bioconversion and agricultural processes simultaneously with a single microreactor is another important direction, investigating synergies between different processes to minimize energy losses and maximize resource utilization. Future work may also include considering emerging advanced reactor designs such as molten salt reactors or liquid metal-cooled reactors that could offer new insights into system compatibility and performance. Identifying the most suitable sites for deploying microreactors is crucial, taking into account factors such as local economy and energy needs, infrastructure, regulations, and geography. Further studies could assess the scalability of integrated systems through pilot-scale demonstrations which may be an important step toward the realization of this technology. Lastly, techno-economic analyses are essential to assessing economic viability and competitiveness, including capital and operating costs, revenue streams, and return on investment.

References

[1] L.K. Almas, W.A. Colette, and Z. Wu, "Declining Ogallala aquifer and Texas panhandle economy," (2004).
[2] IPCC, "IPCC PRESS RELEASE," Https://Www.Ipcc.Ch/Site/Assets/Uploads/2022/04/IPCC_AR6_WGIII_PressRelease_English.Pdf, (2022).
[3] K.S. Birdi, and D.T. Vu, "Wettability and the evaporation rates of fluids from solid surfaces," J Adhes Sci Technol **7**(6), 485–493 (1993).
[4] G.J. Kidron, D.H. Yaalon, and A. Vonshak, "Two causes for runoff initiation on microbiotic crusts: hydrophobicity and pore clogging," Soil Sci **164**(1), 18–27 (1999).
[5] G.J. Burch, I.D. Moore, and J. Burns, "Soil hydrophobic effects on infiltration and catchment runoff," Hydrol Process **3**(3), 211–222 (1989).
[6]"eVinci Microreactor," Https://Www.Westinghousenuclear.Com/Energy-Systems/Evinci-Microreactor, (2024).
[7] P. Zhang, L. Zhang, Y. Chang, M. Xu, Y. Hao, S. Liang, G. Liu, Z. Yang, and C. Wang, "Food-energy-water (FEW) nexus for urban sustainability: A comprehensive review," Resour Conserv Recycl **142**, 215–224 (2019).
[8] V.Z. Schull, B. Daher, M.W. Gitau, S. Mehan, and D.C. Flanagan, "Analyzing FEW nexus modeling tools for water resources decision-making and management applications," Food and Bioproducts Processing **119**, 108–124 (2020).
[9] F. Artioli, M. Acuto, and J. McArthur, "The water-energy-food nexus: An integration agenda and implications for urban governance," Polit Geogr **61**, 215–223 (2017).
[10] R.A. Betts, M. Collins, D.L. Hemming, C.D. Jones, J.A. Lowe, and M.G. Sanderson, "When could global warming reach 4° C?," Philosophical Transactions of the Royal Society A: Mathematical, Physical and Engineering Sciences **369**(1934), 67–84 (2011).
[11] P. Agreement, "Paris agreement," in *Report of the Conference of the Parties to the United Nations Framework Convention on Climate Change (21st Session, 2015: Paris). Retrived December*, (HeinOnline, 2015), p. 2.

[12] L. Chen, G. Msigwa, M. Yang, A.I. Osman, S. Fawzy, D.W. Rooney, and P.-S. Yap, "Strategies to achieve a carbon neutral society: a review," Environ Chem Lett **20**(4), 2277–2310 (2022).

[13] C. Zou, H. Xue, B. Xiong, G. Zhang, S. Pan, C. Jia, Y. Wang, F. Ma, Q. Sun, and C. Guan, "Connotation, innovation and vision of 'carbon neutrality,'" Natural Gas Industry B **8**(5), 523–537 (2021).

[14] S. Qi, *Digital Map of the Aquifer Boundary for the High Plains Aquifer in Parts of Colorado, Kansas, Nebraska, New Mexico, Oklahoma, South Dakota, Texas, and Wyoming* (US Geological Survey, 2010).

[15] C.A. Dieter, M.A. Maupin, R.R. Caldwell, M.A. Harris, T.I. Ivahnenko, J.K. Lovelace, N.L. Barber, and K.S. Linsey, *Estimated Use of Water in the United States in 2015* (US Geological Survey, 2018).

[16] J.M. Deines, A.D. Kendall, M.A. Crowley, J. Rapp, J.A. Cardille, and D.W. Hyndman, "Mapping three decades of annual irrigation across the US High Plains Aquifer using Landsat and Google Earth Engine," Remote Sens Environ **233**, 111400 (2019).

[17] N. Shokri, P. Lehmann, and D. Or, "Characteristics of evaporation from partially wettable porous media," Water Resour Res **45**(2), (2009).

[18] A. Aboubakri, C. Yanik, Y. Akkuş, A. Koşar, and A.K. Sadaghiani, "Numerical and experimental investigation on evaporation of water droplet on surfaces with mixed wettability," in *International Conference on Nanochannels, Microchannels, and Minichannels*, (American Society of Mechanical Engineers, 2020), p. V001T06A002.

[19] C.-C. Hsu, T.-W. Su, C.-H. Wu, L.-S. Kuo, and P.-H. Chen, "Influence of surface temperature and wettability on droplet evaporation," Appl Phys Lett **106**(14), (2015).

[20] A. Jahanbakhsh, O. Shahrokhi, and M.M. Maroto-Valer, "Understanding the role of wettability distribution on pore-filling and displacement patterns in a homogeneous structure via quasi 3D pore-scale modelling," Sci Rep **11**(1), 17847 (2021).

[21] M. Gao, P. Kong, and L. Zhang, "Evaporation dynamics of different sizes sessile droplets on hydrophilic and hydrophobic heating surface under constant wall heat fluxes conditions," International Communications in Heat and Mass Transfer **93**, 93–99 (2018).

[22] D.H. Shin, S.H. Lee, J.-Y. Jung, and J.Y. Yoo, "Evaporating characteristics of sessile droplet on hydrophobic and hydrophilic surfaces," Microelectron Eng **86**(4–6), 1350–1353 (2009).

[23] J.M. Stauber, S.K. Wilson, B.R. Duffy, and K. Sefiane, "Evaporation of droplets on strongly hydrophobic substrates," Langmuir **31**(12), 3653–3660 (2015).
[24] A. Luzar, and K. Leung, "Dynamics of capillary evaporation. I. Effect of morphology of hydrophobic surfaces," J Chem Phys **113**(14), 5836–5844 (2000).
[25] J.D. Holladay, J. Hu, D.L. King, and Y. Wang, "An overview of hydrogen production technologies," Catal Today **139**(4), 244–260 (2009).
[26] P. Sun, and A. Elgowainy, "Updates of hydrogen production from SMR process in GREET® 2019," Argonne National Laboratory: Lemont, IL, USA, (2019).
[27] B. Zohuri, *Nuclear Micro Reactors* (Springer, 2020).
[28] J.R. Philip, and D.A. de De Vries, "Moisture movement in porous materials under temperature gradients," Eos, Transactions American Geophysical Union **38**(2), 222–232 (1957).
[29] A. Cass, G.S. Campbell, and T.L. Jones, "Enhancement of thermal water vapor diffusion in soil," Soil Science Society of America Journal **48**(1), 25–32 (1984).
[30] I. Sakaguchi, T. Momose, and T. Kasubuchi, "Decrease in thermal conductivity with increasing temperature in nearly dry sandy soil," Eur J Soil Sci **58**(1), 92–97 (2007).
[31] X. Pepin, D. Rossetti, S.M. Iveson, and S.J.R. Simons, "Modeling the evolution and rupture of pendular liquid bridges in the presence of large wetting hysteresis," J Colloid Interface Sci **232**(2), 289–297 (2000).
[32] P. Darabi, T. Li, K. Pougatch, M. Salcudean, and D. Grecov, "Modeling the evolution and rupture of stretching pendular liquid bridges," Chem Eng Sci **65**(15), 4472–4483 (2010).
[33] V. Dugas, J. Broutin, and E. Souteyrand, "Droplet evaporation study applied to DNA chip manufacturing," Langmuir **21**(20), 9130–9136 (2005).
[34] M. Chopra, L. Li, H. Hu, M.A. Burns, and R.G. Larson, "DNA molecular configurations in an evaporating droplet near a glass surface," J Rheol (N Y N Y) **47**(5), 1111–1132 (2003).
[35] W. Jia, and H.-H. Qiu, "Experimental investigation of droplet dynamics and heat transfer in spray cooling," Exp Therm Fluid Sci **27**(7), 829–838 (2003).
[36] X. Xu, and L. Ma, "Analysis of the effects of evaporative cooling on the evaporation of liquid droplets using a combined field approach," Sci Rep **5**(1), 8614 (2015).
[37] T. Kawase, H. Sirringhaus, R.H. Friend, and T. Shimoda, "Inkjet printed via-hole interconnections and resistors for all-polymer transistor circuits," Advanced Materials **13**(21), 1601–1605 (2001).

[38] H. Wijshoff, "Drop dynamics in the inkjet printing process," Curr Opin Colloid Interface Sci **36**, 20–27 (2018).
[39] Y. Yu, H. Zhu, J.M. Frantz, M.E. Reding, K.C. Chan, and H.E. Ozkan, "Evaporation and coverage area of pesticide droplets on hairy and waxy leaves," Biosyst Eng **104**(3), 324–334 (2009).
[40] Y. Luo, D.R. Miller, X. Yang, M.L. Mcmanus, and H.M. Krider, "Characteristics of evaporation from water-based bacterial pesticide droplets," Transactions of the ASAE **37**(5), 1473–1479 (1994).
[41] M. Kimura, M.J. Misner, T. Xu, S.H. Kim, and T.P. Russell, "Long-range ordering of diblock copolymers induced by droplet pinning," Langmuir **19**(23), 9910–9913 (2003).
[42] A. Jaworek, "Electrospray droplet sources for thin film deposition," J Mater Sci **42**, 266–297 (2007).
[43] R.D. Deegan, O. Bakajin, T.F. Dupont, G. Huber, S.R. Nagel, and T.A. Witten, "Capillary flow as the cause of ring stains from dried liquid drops," Nature **389**(6653), 827–829 (1997).
[44] J. Berg, *Wettability* (CRC Press, 1993).
[45] C. Della Volpe, and S. Siboni, "Use, abuse, misuse and proper use of contact angles: a critical review," Reviews of Adhesion and Adhesives **3**(4), 365–385 (2015).
[46] A. Marmur, "Hydro-hygro-oleo-omni-phobic? Terminology of wettability classification," Soft Matter **8**(26), 6867–6870 (2012).
[47] J. Drelich, "Guidelines to measurements of reproducible contact angles using a sessile-drop technique," Surf Innov **1**(4), 248–254 (2013).
[48] H. Li, A. Li, Z. Zhao, M. Li, and Y. Song, "Heterogeneous wettability surfaces: Principle, construction, and applications," Small Struct **1**(2), 2000028 (2020).
[49] Y. Wu, T. Hang, Z. Yu, L. Xu, and M. Li, "Lotus leaf-like dual-scale silver film applied as a superhydrophobic and self-cleaning substrate," Chemical Communications **50**(61), 8405–8407 (2014).
[50] M. Kuang, L. Wang, and Y. Song, "Controllable printing droplets for high-resolution patterns," Advanced Materials **26**(40), 6950–6958 (2014).
[51] A.R. Betz, J. Jenkins, and D. Attinger, "Boiling heat transfer on superhydrophilic, superhydrophobic, and superbiphilic surfaces," Int J Heat Mass Transf **57**(2), 733–741 (2013).

[52] M.M. Derby, A. Chatterjee, Y. Peles, and M.K. Jensen, “Flow condensation heat transfer enhancement in a mini-channel with hydrophobic and hydrophilic patterns,” Int J Heat Mass Transf **68**, 151–160 (2014).
[53] P.P. Chakraborty, R. Huber, X. Chen, and M.M. Derby, “Evaporation from simulated soil pores: effects of wettability, liquid islands, and breakup,” Interfacial Phenom Heat Transf **6**(4), (2018).
[54] P. Ustohal, F. Stauffer, and T. Dracos, “Measurement and modeling of hydraulic characteristics of unsaturated porous media with mixed wettability,” J Contam Hydrol **33**(1–2), 5–37 (1998).
[55] R.G. Picknett, and R. Bexon, “The evaporation of sessile or pendant drops in still air,” J Colloid Interface Sci **61**(2), 336–350 (1977).
[56] M.E.R. Shanahan, “Simple theory of" stick-slip" wetting hysteresis,” Langmuir **11**(3), 1041–1043 (1995).
[57] A.G. Sourais, I.E. Markodimitrakis, N.T. Chamakos, and A.G. Papathanasiou, “Droplet evaporation dynamics on heterogeneous surfaces: Numerical modeling of the stick-slip motion,” Int J Heat Mass Transf **207**, 123992 (2023).
[58] S. Dash, and S. V Garimella, “Droplet evaporation dynamics on a superhydrophobic surface with negligible hysteresis,” Langmuir **29**(34), 10785–10795 (2013).
[59] T.D. Blake, and J. De Coninck, “The influence of solid–liquid interactions on dynamic wetting,” Adv Colloid Interface Sci **96**(1–3), 21–36 (2002).
[60] D. Orejon, K. Sefiane, and M.E.R. Shanahan, “Stick–slip of evaporating droplets: substrate hydrophobicity and nanoparticle concentration,” Langmuir **27**(21), 12834–12843 (2011).
[61] F. Schönfeld, K.-H. Graf, S. Hardt, and H.-J. Butt, “Evaporation dynamics of sessile liquid drops in still air with constant contact radius,” Int J Heat Mass Transf **51**(13), 3696–3699 (2008).
[62] J. Pakkebier, P.P. Chakraborty, and M.M. Derby, “Effects of heterogenous wettability on evaporation from a simulated soil pore: Stick-slip evaporative mode and contact line motion,” AIP Adv **14**(3), 035127 (2024).
[63] H.Y. Erbil, “Evaporation of pure liquid sessile and spherical suspended drops: A review,” Adv Colloid Interface Sci **170**(1–2), 67–86 (2012).
[64] T. Chen, M.-S. Chiu, and C.-N. Weng, “Derivation of the generalized Young-Laplace equation of curved interfaces in nanoscaled solids,” J Appl Phys **100**(7), (2006).

[65] C.W. Extrand, and S.I. Moon, “Contact angles on spherical surfaces,” Langmuir **24**(17), 9470–9473 (2008).
[66] A. Marmur, and B. Krasovitski, “Line tension on curved surfaces: Liquid drops on solid micro-and nanospheres,” Langmuir **18**(23), 8919–8923 (2002).
[67] C. Gögelein, M. Brinkmann, M. Schröter, and S. Herminghaus, “Controlling the formation of capillary bridges in binary liquid mixtures,” Langmuir **26**(22), 17184–17189 (2010).
[68] A.P. Willard, and D. Chandler, “The molecular structure of the interface between water and a hydrophobic substrate is liquid-vapor like,” J Chem Phys **141**(18), (2014).
[69] G. Viswanadam, and G.G. Chase, “Contact angles of drops on curved superhydrophobic surfaces,” J Colloid Interface Sci **367**(1), 472–477 (2012).
[70] D. Wu, P. Wang, P. Wu, Q. Yang, F. Liu, Y. Han, F. Xu, and L. Wang, “Determination of contact angle of droplet on convex and concave spherical surfaces,” Chem Phys **457**, 63–69 (2015).
[71] F.A.L. Dullien, *Porous Media: Fluid Transport and Pore Structure* (Academic press, 2012).
[72] H.S. Rabbani, B. Zhao, R. Juanes, and N. Shokri, “Pore geometry control of apparent wetting in porous media,” Sci Rep **8**(1), 15729 (2018).
[73] A. Nabizadeh, H. Hassanzadeh, M. Sharifi, and M.K. Moraveji, “Effects of dynamic contact angle on immiscible two-phase flow displacement in angular pores: A computational fluid dynamics approach,” J Mol Liq **292**, 111457 (2019).
[74] A. Peakman, Z. Hodgson, and B. Merk, “Advanced micro-reactor concepts,” Progress in Nuclear Energy **107**, 61–70 (2018).
[75] G. Black, D. Shropshire, K. Araújo, and A. van Heek, “Prospects for nuclear microreactors: A review of the technology, economics, and regulatory considerations,” Nucl Technol **209**(sup1), S1–S20 (2023).
[76] Z. Zhang, C. Wang, K. Guo, S. Qiu, G.H. Su, and W. Tian, “Microreactors,” in *Nuclear Power Reactor Designs*, (Elsevier, 2024), pp. 309–347.
[77] D. Kalinichenko, L. Wodrich, A.J.H. Lee, T. Kozlowski, and C.S. Brooks, “Analysis of nuclear microreactor efficacy with hydrogen production methods,” Progress in Nuclear Energy **168**, 104994 (2024).
[78] D.P. Guillen, “Review of Passive Heat Removal Strategies for Nuclear Microreactor Systems,” Nucl Technol **209**(sup1), S21–S40 (2023).

[79]"Reactor: Xe-Mobile," Https://X-Energy.Com/Reactors/Xe-Mobile, (2024).
[80]"Small Nuclear Power Reactors," Https://Www.World-Nuclear.Org/Information-Library/Nuclear-Fuel-Cycle/Nuclear-Power-Reactors/Small-Nuclear-Power-Reactors.Aspx, (2024).
[81] R. Testoni, A. Bersano, and S. Segantin, "Review of nuclear microreactors: Status, potentialities and challenges," Progress in Nuclear Energy **138**, 103822 (2021).
[82]"Aurora-Oklo Application," Https://Www.Nrc.Gov/Reactors/New-Reactors/Large-Lwr/Col/Aurora-Oklo.Html, (2020).
[83]"holosgen.com," Https://Www.Holosgen.Com/Holos-Quad/, (2017).
[84] N. Stauff, C.H. Lee, and C. Filippone, *Core Design of the Holos-Quad Microreactor* (Argonne National Lab.(ANL), Argonne, IL (United States), 2022).
[85] U-Battery, "A differentiated small modular reactor offering providing low cost, low risk, low carbon off-grid energy with a high heat output," Https://Www.u-Battery.Com/Cdn/Uploads/Supporting-Files/U-Battery_2-Pager_handout_final.Pdf, (2023).
[86]"u-battery.com," Https://Www.u-Battery.Com/Cdn/Uploads/Supporting-Files/U-Battery_brochure_Feb21.Pdf, (2019).
[87]"usnc.com," Https://Www.Usnc.Com/Mmr/, (2024).
[88] B.H. Yan, C. Wang, and L.G. Li, "The technology of micro heat pipe cooled reactor: A review," Ann Nucl Energy **135**, 106948 (2020).
[89]"Statement: U-Battery," Https://Www.Urenco.Com/News/Global/2023/Statement-u-Battery, (2023).
[90]"nrc.gov," Https://Www.Nrc.Gov/Docs/ML2135/ML21357A034.Pdf, (2022).
[91]"eia.gov," Https://Www.Eia.Gov/Energyexplained/Electricity/Electricity-in-the-Us.Php, (2023).
[92] International Energy Agency (IEA), "Global forecast summary," Https://Www.Iea.Org/Reports/Renewables-2023/Electricity, (2023).
[93] D.A.J. Rand, and R.M. Dell, "FUELS – HYDROGEN PRODUCTION | Coal Gasification," in *Encyclopedia of Electrochemical Power Sources*, edited by J. Garche, (Elsevier, Amsterdam, 2009), pp. 276–292.
[94] Y. Zhang, Y. Cui, P. Chen, S. Liu, N. Zhou, K. Ding, L. Fan, P. Peng, M. Min, Y. Cheng, Y. Wang, Y. Wan, Y. Liu, B. Li, and R. Ruan, "Chapter 14 - Gasification Technologies and Their

Energy Potentials," in *Sustainable Resource Recovery and Zero Waste Approaches*, edited by M.J. Taherzadeh, K. Bolton, J. Wong, and A. Pandey, (Elsevier, 2019), pp. 193–206.
[95]"netl.doe.gov," Https://Www.Netl.Doe.Gov/Research/Coal/Energy-Systems/Gasification/Gasifipedia/Syngas-Composition, (n.d.).
[96] P. De Filippis, M. Scarsella, B. de Caprariis, and R. Uccellari, "Biomass gasification plant and syngas clean-up system," Energy Procedia **75**, 240–245 (2015).
[97] M. Speidel, G. Kraaij, and A. Wörner, "A new process concept for highly efficient conversion of sewage sludge by combined fermentation and gasification and power generation in a hybrid system consisting of a SOFC and a gas turbine," Energy Convers Manag **98**, 259–267 (2015).
[98] M. Pecchi, and M. Baratieri, "Coupling anaerobic digestion with gasification, pyrolysis or hydrothermal carbonization: a review," Renewable and Sustainable Energy Reviews **105**, 462–475 (2019).
[99] M.M. Yung, A.R. Stanton, K. Iisa, R.J. French, K.A. Orton, and K.A. Magrini, "Multiscale evaluation of catalytic upgrading of biomass pyrolysis vapors on Ni-and Ga-modified ZSM-5," Energy & Fuels **30**(11), 9471–9479 (2016).
[100] R. Sakthivel, H. Abbhijith, G. V Harshini, M.S. Vardhan, and K.P. Shadangi, "Biofuels: Classification, conversion technologies, optimization techniques and applications," in *Biorefineries: Production of Fuels and Platform Chemicals*, (2024), pp. 1–30.
[101]"ars.usda.gov," Https://Www.Ars.Usda.Gov/Northeast-Area/Wyndmoor-Pa/Eastern-Regional-Research-Center/Docs/Biomass-Pyrolysis-Research-1/What-Is-Pyrolysis/, (2021).
[102] N.D. Berge, K.S. Ro, J. Mao, J.R. V Flora, M.A. Chappell, and S. Bae, "Hydrothermal carbonization of municipal waste streams," Environ Sci Technol **45**(13), 5696–5703 (2011).
[103] A. Funke, and F. Ziegler, "Hydrothermal carbonization of biomass: A summary and discussion of chemical mechanisms for process engineering," Biofuels, Bioproducts and Biorefining **4**(2), 160–177 (2010).
[104] M.T. Reza, J. Andert, B. Wirth, D. Busch, J. Pielert, J.G. Lynam, and J. Mumme, "Hydrothermal carbonization of biomass for energy and crop production," Appl. Bioenergy **1**(1), 11–29 (2014).
[105] Y.-H. Xu, and M.-F. Li, "Hydrothermal liquefaction of lignocellulose for value-added products: Mechanism, parameter and production application," Bioresour Technol **342**, 126035 (2021).

[106] I. Sharma, D. Rackemann, J. Ramirez, D.J. Cronin, L. Moghaddam, J.N. Beltramini, J. Te'o, K. Li, C. Shi, and W.O.S. Doherty, "Exploring the potential for biomethane production by the hybrid anaerobic digestion and hydrothermal gasification process: A review," J Clean Prod **362**, 132507 (2022).
[107] A.R.K. Gollakota, N. Kishore, and S. Gu, "A review on hydrothermal liquefaction of biomass," Renewable and Sustainable Energy Reviews **81**, 1378–1392 (2018).
[108] S.S. Toor, L. Rosendahl, and A. Rudolf, "Hydrothermal liquefaction of biomass: a review of subcritical water technologies," Energy **36**(5), 2328–2342 (2011).
[109] Y. Tian, F. Wang, J.O. Djandja, S.-L. Zhang, Y.-P. Xu, and P.-G. Duan, "Hydrothermal liquefaction of crop straws: Effect of feedstock composition," Fuel **265**, 116946 (2020).
[110] C. He, C.-L. Chen, A. Giannis, Y. Yang, and J.-Y. Wang, "Hydrothermal gasification of sewage sludge and model compounds for renewable hydrogen production: a review," Renewable and Sustainable Energy Reviews **39**, 1127–1142 (2014).
[111]"grtgaz.com," Https://Www.Grtgaz.Com/En/Ourenergies/Wet-Waste/Hydrothermal-Gasification-5-Points#:~:Text=How%20does%20Hydrothermal%20Gasification%20work,CO2%20(Carbon%20dioxide)., (n.d.).
[112] A. Kruse, "Supercritical water gasification," Biofuels, Bioproducts and Biorefining: Innovation for a Sustainable Economy **2**(5), 415–437 (2008).
[113] C.A. Cardona, and Ó.J. Sánchez, "Fuel ethanol production: process design trends and integration opportunities," Bioresour Technol **98**(12), 2415–2457 (2007).
[114] A. Abreu-Cavalheiro, and G. Monteiro, "Solving ethanol production problems with genetically modified yeast strains," Brazilian Journal of Microbiology **44**, 665–671 (2013).
[115] H. Zabed, J.N. Sahu, A. Suely, A.N. Boyce, and G. Faruq, "Bioethanol production from renewable sources: Current perspectives and technological progress," Renewable and Sustainable Energy Reviews **71**, 475–501 (2017).
[116] Y. Chen, J.J. Cheng, and K.S. Creamer, "Inhibition of anaerobic digestion process: a review," Bioresour Technol **99**(10), 4044–4064 (2008).
[117] B.-Q. Liao, J.T. Kraemer, and D.M. Bagley, "Anaerobic membrane bioreactors: applications and research directions," Crit Rev Environ Sci Technol **36**(6), 489–530 (2006).

[118] J. Tang, Y. Pu, T. Zeng, Y. Hu, J. Huang, S. Pan, X.C. Wang, Y. Li, and A.E.-F. Abomohra, "Enhanced methane production coupled with livestock wastewater treatment using anaerobic membrane bioreactor: Performance and membrane filtration properties," Bioresour Technol **345**, 126470 (2022).

[119] D.P. Chynoweth, "Anaerobic digestion of biomass," (1987).

[120] G.J. Swart, C.M. Blignaut, and P.J. Jooste, "PASTEURIZATION | Other Pasteurization Processes," in *Encyclopedia of Food Sciences and Nutrition (Second Edition)*, edited by B. Caballero, (Academic Press, Oxford, 2003), pp. 4401–4406.

[121]"vdh.virginia.gov," Https://Www.Vdh.Virginia.Gov/Environmental-Health/Food-Safety-in-Virginia/Milk-Safety/Pasteurization/#:~:Text=Batch%20pasteurization%20involves%20heating%20every,%C2%B0F%20for%2015%20seconds., (n.d.).

[122] S.W. Lee, Y. Lee, N. Kim, and H. Jo, "Design of heat pipe cooled microreactor based on cycle analysis and evaluation of applicability for remote regions," Energy Convers Manag **288**, 117126 (2023).

[123] L. Drbal, K. Westra, and P. Boston, *Power Plant Engineering* (Springer Science & Business Media, 2012).

[124] G. Xiao, T. Yang, H. Liu, D. Ni, M.L. Ferrari, M. Li, Z. Luo, K. Cen, and M. Ni, "Recuperators for micro gas turbines: A review," Appl Energy **197**, 83–99 (2017).

[125] B.L. Boissevain, P.E. Zemke, and B.D. Wood, "Improving energy utilization in anaerobic digester power systems," Biol Eng Trans **6**(1), 43–56 (2013).

[126] A. Pattiya, S. Sukkasi, and V. Goodwin, "Fast pyrolysis of sugarcane and cassava residues in a free-fall reactor," Energy **44**(1), 1067–1077 (2012).

[127] M.J. Moran, H.N. Shapiro, D.D. Boettner, and M.B. Bailey, *Fundamentals of Engineering Thermodynamics* (John Wiley & Sons, 2010).

Appendix A - Wettability Data

This appendix shows the additional experimental trials for each wettability configuration not depicted in the main text. This includes images similar to Fig. 2.2, where the initial droplet placement, the droplet immediately before liquid island formation, and the droplet immediately after liquid island formation are shown.

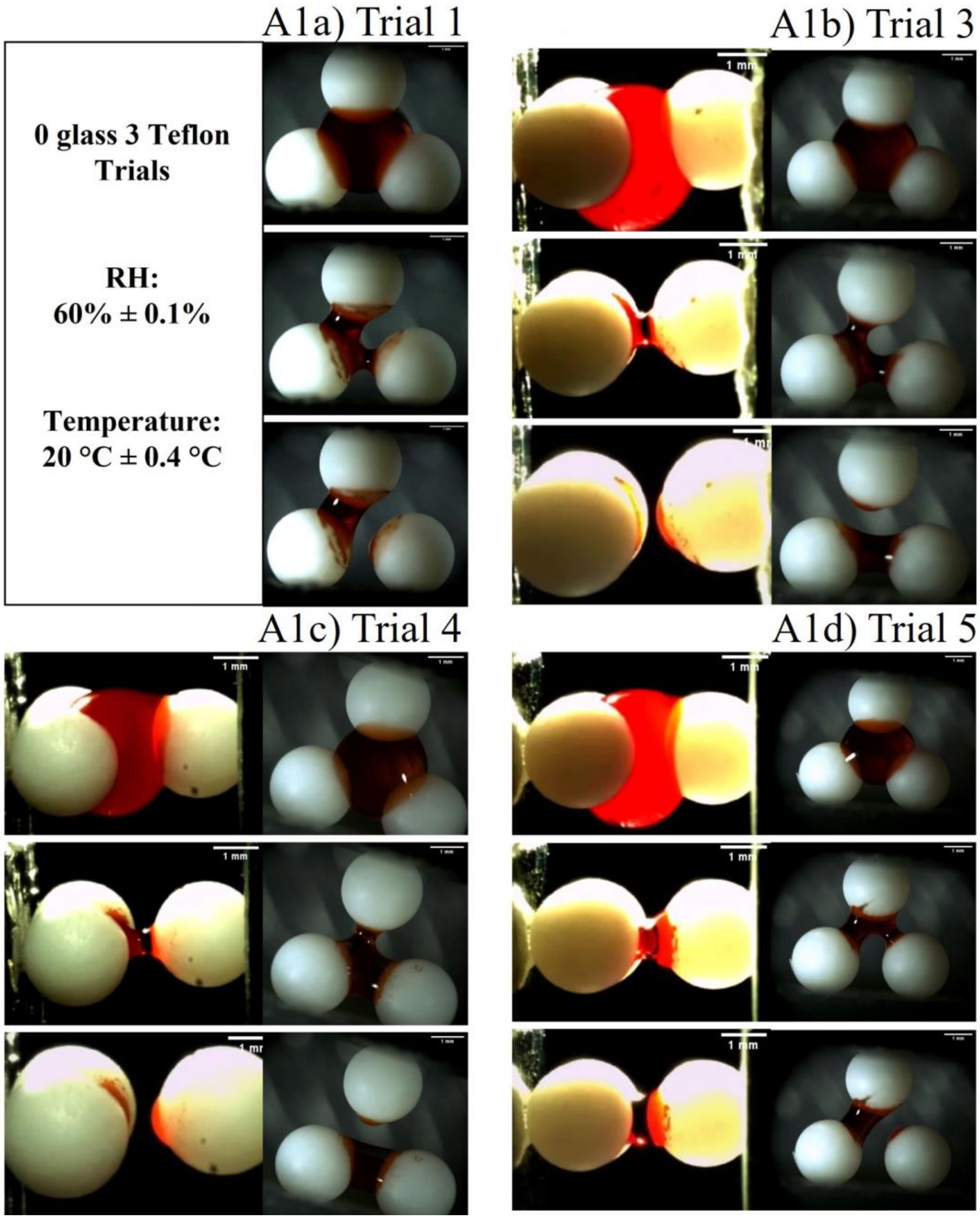

Appendix Figure A.1: Additional 0 glass 3 Teflon trials conducted that show initial droplet placement, immediately before liquid island formation, and immediately after liquid island formation inside of the simulated soil pore. A1a) depicts trial 1, A1b) depicts trial 3, A1c) depicts trial 4, and A1d) depicts trial 5. Trial 2 is shown in Figure 2.2d in the main text. Trial 1 does not have side camera footage.

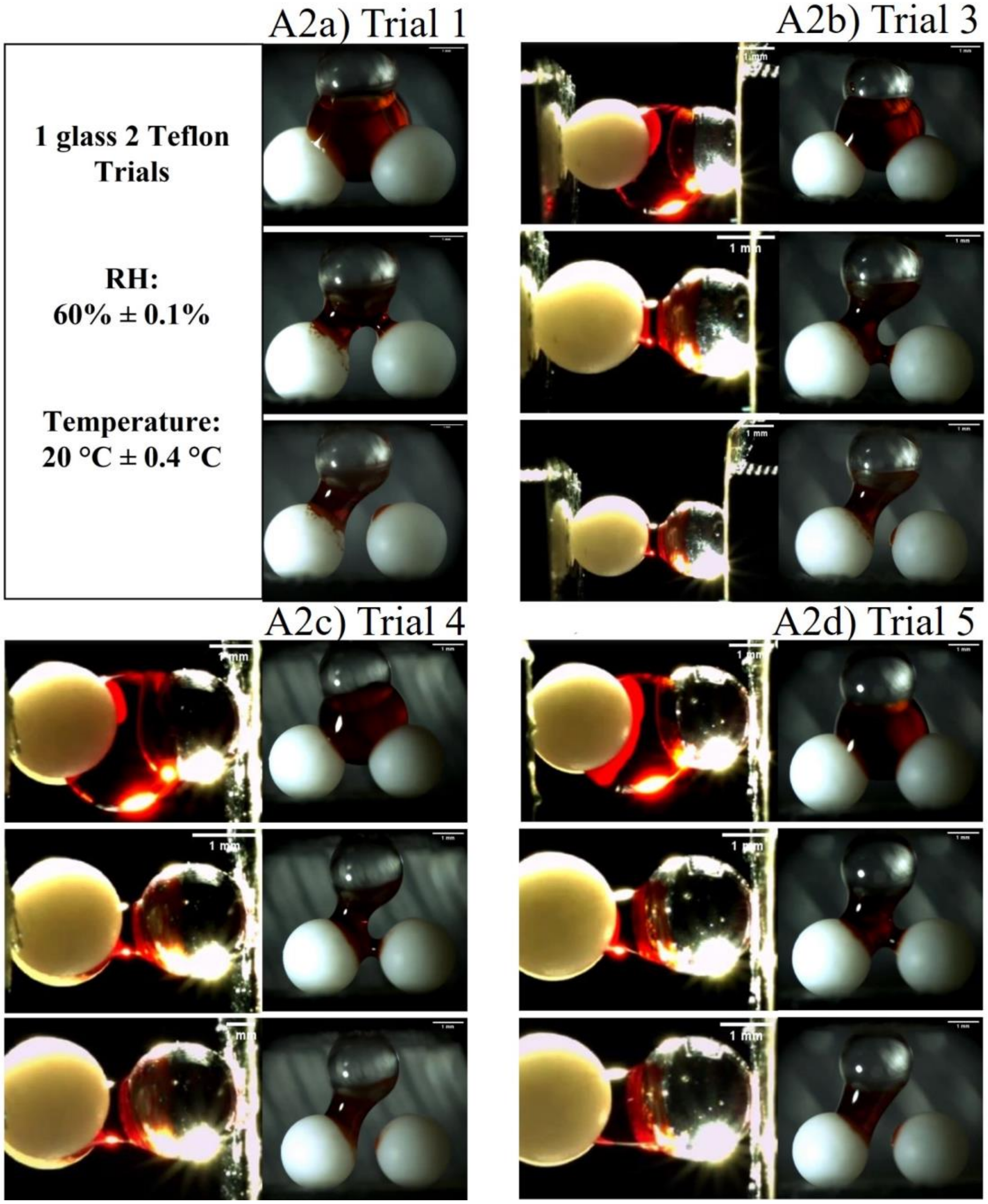

Appendix Figure A.2: Additional 1 glass 2 Teflon trials conducted that show initial droplet placement, immediately before liquid island formation, and immediately after liquid island formation inside of the simulated soil pore. A2a) depicts trial 1, A2b) depicts trial 3, A2c) depicts trial 4, and A2d) depicts trial 5. Trial 2 is shown in Figure 2.2c in the main text. Trial 1 does not have side camera footage.

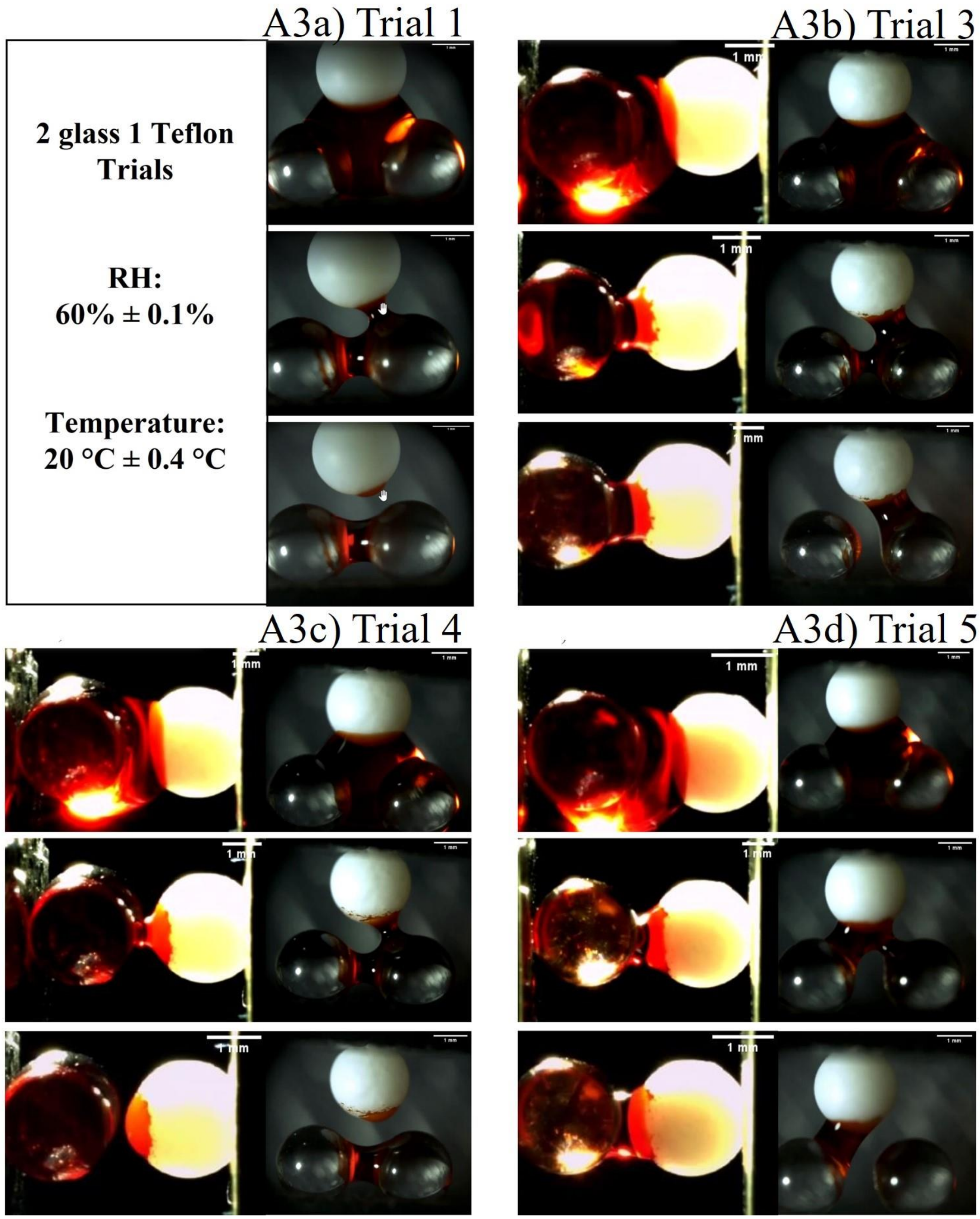

Appendix Figure A.3: Additional 2 glass 1 Teflon trials conducted that show initial droplet placement, immediately before liquid island formation, and immediately after liquid island formation inside of the simulated soil pore. A3a) depicts trial 1, A3b) depicts trial 3, A3c) depicts trial 4, and A3d) depicts trial 5. Trial 2 is shown in Figure 2.2b in the main text. Trial 1 does not have side camera footage.

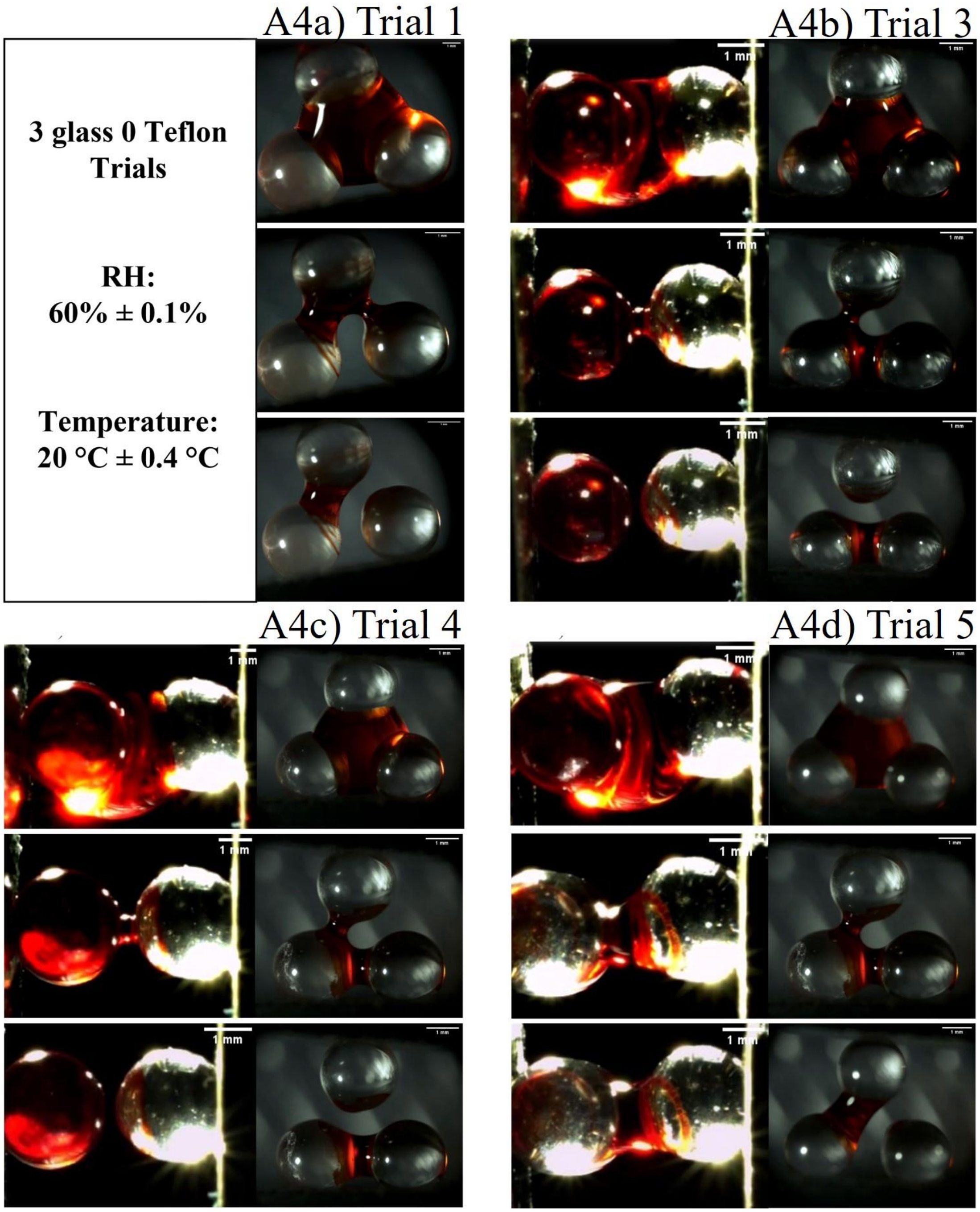

Appendix Figure A.4: Additional 3 glass 0 Teflon trials conducted that show initial droplet placement, immediately before liquid island formation, and immediately after liquid island formation inside of the simulated soil pore. A4a) depicts trial 1, A4b) depicts trial 3, A4c) depicts trial 4, and A4d) depicts trial 5. Trial 2 is shown in Figure 2.2a in the main text. Trial 1 does not have side camera footage.

Appendix B - Nuclear Microreactor Feasibility Data

The following lines are the code input into EES to build the model and collect data:

```
{State 1: Ambient}
T1=293.15 [K] {Compressor inlet temperature}
h1=enthalpy(Air,T=T1)
s1=entropy(Air,T=T1,P=P1)
P1=101325 [Pa]

{State 2: After compressor}
P2= 365057 [Pa] {set as parametric value to get eta_net=0.36}
h2s=enthalpy(Air,P=P2,s=s1)
h2=((h2s-h1)/eta_compressor)+H1
T2=temperature(Air,h=H2)

{State x: After Regenerator}
Px=P2 {Assumed no pressure drop through heat exchangers}
Tx=temperature(Air,h=hx)
epsilon_reg=0.9 {Powerplant engineering reference}
hx=(epsilon_reg*(H_beta-H2))+H2

{State 3: After IHX 1}
T3=873.2 [K] {Process heat available from eVinci microreactor}
```

```
h3=enthalpy(Air,T=T3)
P3=P2
s3=entropy(Air,T=T3,P=P3)
{State alpha: Position 1}
P_alpha=P3
Tp=873.2 [K] {Set for the various processes, parametric value}
T_alpha=T3-(bigc_pair/bigc_pc)*(Tp-Ta) {Simplified from heat exchanger effectiveness}
Q_dot_p=Q_dot_out {All of what leaves is given to process}
Q_dot_p=m_dot_p*(hp-ha) {Calculates m_dot_p}
hp=enthalpy(Air,T=Tp)
Ta=T1
ha=enthalpy(Air,T=Ta)
h_alpha=enthalpy(Air,T=T_alpha)
s_alpha=entropy(Air,T=T_alpha,P=P_alpha)
Q_dot_out=m_dot*(h3-h_alpha) {Heat expended powering concurrent process}
epsilon_HTX=(bigc_pc*(Tp-Ta))/(bigc_pair*(T3-Ta))
{Position 2 and 3}
"h_alpha=h3
s_alpha=s3
P_alpha=P3"
```

```
{State 4: After Turbine}

P4=P1
h4=-eta_turbine*(h_alpha-h4s)+h_alpha
h4s=enthalpy(Air,P=P4,s=s_alpha)
T4=temperature(Air,h=h4)

{State beta: Position 2}

"Q_dot_out=m_dot*(h4-h_beta) {Heat expended powering concurrent process}
Tp=513 {Set for various processes, parametric value}
T_beta=T4-(bigc_pair/bigc_pc)*(Tp-Ta) {Simplified from heat exchanger effectiveness}
Q_dot_p=Q_dot_out {All of what leaves is given to process}
Q_dot_p=m_dot_p*(hp-ha) {Calculates m_dot_p}
hp=enthalpy(Air,T=Tp)
Ta=T1 [K]
ha=enthalpy(Air,T=Ta)
h_beta=enthalpy(Air,T=T_beta)
P_beta=P1 [Pa]
epsilon_HTX=(bigc_pc*(Tp-Ta))/(bigc_pair*(T4-T_beta))"
{Position 1 and 3}
h_beta=h4
```

```
s_beta=h4
P_beta=P1
{State y: After regenerator}
Ty=temperature(Air,h=hy)
hy=h2+h_beta-hx {Can use epsilon or also first law to solve for Hy (energy balance)}
Py=P1
{State gamma: Position 3}
"Q_dot_out=m_dot*(hy-h_gamma) {Heat expended powering concurrent process}
Tp=873.2 {Set for various processes, parametric value}
T_gamma=Ty-(bigc_pair/bigc_pc)*(Tp-Ta) {Simplified from heat exchanger effectiveness}
Q_dot_p=Q_dot_out {All of what leaves is given to process}
Q_dot_p=m_dot_p*(hp-ha) {Calculates m_dot_p}
hp=enthalpy(Air,T=Tp)
Ta=T1 [K]
ha=enthalpy(Air,T=Ta)
h_gamma=enthalpy(Air,T=T_gamma)
epsilon_HTX=(bigc_pc*(Tp-Ta))/(bigc_pair*(Ty-T_gamma))"
```

88. {Misc.}

89. eta_cycle=((h_alpha-h4)-(h2-h1))/(h3-hx)

90. eta_turbine=0.92 {Powerplant engineering reference}

91. eta_compressor=0.85 {Powerplant engineering reference}

92.

93. Q_dot_in=13000 [kW] {Thermal heat from eVinci microreactor}

94. m_dot=Q_dot_in/(h3-hx) {kg/s}

95.

96. W_dot_turbine=m_dot*(h_alpha-h4) {kW}

97. W_dot_compressor=m_dot*(h2-h1)

98. eta_carnot=1-(T1/T3)

99. P_ratio=P2/P1

100.

101. W_dot_net=W_dot_turbine-W_dot_compressor {kW}

102.

103. {Specific Heats, select for desired process}

104. "c_pc=3.94" {Pasteurization,milk}

105. "c_pc=Cp(Water,T=Tp,P=P1+20000)" {AD, up to 0.2 bar over atmospheric}

106. "c_pc=Cp(Water,T=Tp,P=5E6)" {Ethanol, 5MPa pressure optimal}

107. "c_pc=Cp(Water,T=Tp,P=6E6)" {HTC, 6Mpa is average}

108. "c_pc=Cp(Water,T=Tp,P=12.5E6)" {HTL}

109. "c_pc=Cp(N2,T=Tp)" {Pyrolysis}

110. "c_pc=Cp(Water,T=Tp,P=25.5E6)" {HTG}

111. c_pc=SpecHeat(Air,T=Tp) {Gasification}

112. c_pair=SpecHeat(Air,T=T3) {Change based on position}

113. bigc_pc=c_pc*m_dot_p

114. bigc_pair=c_pair*m_dot